



PRIFYSGOL
BANGOR
UNIVERSITY

Stripping back the modern to reveal the Cenomanian-Turonian climate and temperature gradient underneath

Laugie, Marie ; Donnadieu, Yannick; Ladant, Jean-Baptiste; Green, Mattias; Bopp, Laurent; Raison, Francois

Climate of the Past

DOI:

[10.5194/cp-16-953-2020](https://doi.org/10.5194/cp-16-953-2020)

Published: 05/06/2020

Peer reviewed version

[Cyswllt i'r cyhoeddiad / Link to publication](#)

Dyfyniad o'r fersiwn a gyhoeddwyd / Citation for published version (APA):

Laugie, M., Donnadieu, Y., Ladant, J-B., Green, M., Bopp, L., & Raison, F. (2020). Stripping back the modern to reveal the Cenomanian-Turonian climate and temperature gradient underneath. *Climate of the Past*, 16(3), 953–971. <https://doi.org/10.5194/cp-16-953-2020>

Hawliau Cyffredinol / General rights

Copyright and moral rights for the publications made accessible in the public portal are retained by the authors and/or other copyright owners and it is a condition of accessing publications that users recognise and abide by the legal requirements associated with these rights.

- Users may download and print one copy of any publication from the public portal for the purpose of private study or research.
- You may not further distribute the material or use it for any profit-making activity or commercial gain
- You may freely distribute the URL identifying the publication in the public portal ?

Take down policy

If you believe that this document breaches copyright please contact us providing details, and we will remove access to the work immediately and investigate your claim.

1 Stripping back the Modern to reveal the Cenomanian-Turonian climate and the 2 temperature gradient underneath

3 Marie Laugie¹, Yannick Donnadiou¹, Jean-Baptiste Ladant², Mattias Green³, Laurent Bopp^{4,5} and François Raison⁶.

4 ¹Aix Marseille Univ, CNRS, IRD, INRA, Coll. France, CEREGE, Aix-en-Provence, France

5 ²Department of Earth and Environmental Sciences, University of Michigan, Ann Arbor, MI, USA

6 ³School of Ocean Sciences, Bangor University, Menai Bridge, UK

7 ⁴Ecole Normale Supérieure (ENS Paris) - Département des Géosciences - France

8 ⁵Laboratoire de Météorologie Dynamique (UMR 8539) (LMD) - Université Pierre et Marie Curie -

9 Paris 6, Institut national des sciences de l'Univers, École Polytechnique, École des Ponts ParisTech,

10 Centre National de la Recherche Scientifique : UMR8539, École Normale Supérieure - Paris - France

11 ⁶Total EP – R&D Frontier Exploration - France

12 ABSTRACT

13 During past geological times, the Earth experienced several intervals of global warmth, but their driving
14 factors remain equivocal. A careful appraisal of the main processes involved in these controlling past warm events
15 is essential to ~~evaluate how they can~~ inform future climates and ultimately provide decision makers with a clear
16 understanding of the processes at play in a warmer world. In this context, intervals of greenhouse climates, such
17 as the thermal maximum of the Cenomanian-Turonian (~94 Ma) during the Cretaceous period, are of particular
18 interest. Here we use the IPSL-CM5A2 Earth System Model to unravel the forcing parameters of the Cenomanian-
19 Turonian greenhouse climate. We perform six simulations with an incremental change in five major boundary
20 conditions in order to isolate their respective role on climate change between the Cenomanian-Turonian and the
21 preindustrial. Starting with a preindustrial simulation, we implement the following changes in boundary
22 conditions: (1) the absence of polar ice sheets, (2) the increase in atmospheric $p\text{CO}_2$ to 1120 ppm, (3) the change
23 of vegetation and soil parameters, (4) the 1% decrease in the Cenomanian-Turonian value of the solar constant
24 and (5) the Cenomanian-Turonian paleogeography. Between the preindustrial simulation and the Cretaceous
25 simulation, the model simulates a global warming of more than 11°C. Most of this warming is driven by the
26 increase in atmospheric $p\text{CO}_2$ to 1120 ppm. Paleogeographic changes represent the second major contributor to
27 global warming, while whereas the reduction in the solar constant counteracts most of geographically-driven
28 global warming. We further demonstrate that the implementation of Cenomanian-Turonian boundary conditions
29 flattens meridional temperature gradients compared to in the preindustrial simulation. Interestingly, we show
30 that paleogeography is the major driver of the flattening in the low- to mid-latitudes, whereas $p\text{CO}_2$ rise and polar
31 ice sheet retreat dominate the high-latitude response.

1. INTRODUCTION

The Cretaceous period is of particular interest to understand drivers of past greenhouse climates because intervals of prolonged global warmth (O'Brien et al. 2017, Huber et al. 2018) and elevated atmospheric CO₂ levels (Wang et al., 2014), possibly similar to future levels, have been documented in the proxy record. The thermal maximum of the Cenomanian-Turonian (CT) interval (94 Ma) represents the acme of Cretaceous warmth, during which one of the most important carbon cycle perturbations of the Phanerozoic occurred: the oceanic anoxic event 2 (OAE2). Valuable understanding of what controls large-scale climate processes can hence be drawn from investigations of the mechanisms responsible for the CT thermal maximum and carbon cycle perturbation.

Proxy-based reconstructions and model simulations of sea-surface temperatures (SST) for the CT reveal that during OAE2 the equatorial Atlantic was 4-6° warmer than today (Norris et al., 2002; Bice et al., 2006; Pucéat et al., 2007; Tabor et al., 2016), and possibly even warmer than that (6-9° - Forster et al., 2007). This short and abrupt episode of major climatic, oceanographic, and global carbon cycle perturbations occurred at the CT Boundary and was superimposed on a long period of global warmth (Jenkyns, 2010). The high latitudes were also much warmer than today (Herman and Spicer, 2010; Spicer and Herman, 2010), as was the abyssal ocean which experienced bottom temperatures reaching up to 20°C during the CT (Huber et al., 2002; Littler et al., 2011; Friedrich et al., 2012). Paleobotanical studies suggest that the atmosphere was also much warmer (Herman and Spicer, 1996), with high-latitude temperatures up to 17°C higher than today (Herman and Spicer, 2010) and possibly reaching annual means of 10-12°C in Antarctica (Huber et al., 1999).

The steepness of the equator-to-pole gradient is still a matter of debate, in particular because of inconsistencies between data and models as the latter usually predict steeper gradients than those reconstructed from proxy data (Barron, 1993; Huber et al., 1995; Heinemann et al., 2009; Tabor et al., 2016). Models and data generally agree, however, that Cretaceous sea-surface temperature (SST) gradients were reduced compared to today (Sellwood et al., 1994; Huber et al., 1995; Jenkyns et al., 2004; O'Brien et al., 2017; Robinson et al., 2019).

The main factor generally considered responsible for the Cretaceous global warm climate is the higher atmospheric CO₂ concentration (Barron et al., 1995; Crowley and Berner, 2001; Royer et al., 2007; Wang et al., 2014; Foster et al., 2017). This has been determined by proxy-data reconstructions of the Cretaceous

Commented [MG1]: I think we need a reference here

61 $p\text{CO}_2$ using various techniques, including analysis of paleosols $\delta^{13}\text{C}$ (Sandler and Harlavan, 2006; Leier et al., 2009;
62 Hong and Lee, 2012), liverworts $\delta^{13}\text{C}$ (Fletcher et al., 2006) or phytane $\delta^{13}\text{C}$ (Damsté et al., 2008; Van Bentum et
63 al., 2012) and leaf stomata analysis (Barclay et al., 2010; Mays et al., 2015; Retallack and Conde, 2020). Modelling
64 studies have also focused on estimating Cretaceous atmospheric CO_2 levels (Barron et al., 1995; Poulsen et al.,
65 2001, 2007; Berner, 2006; Bice et al., 2006; Monteiro et al., 2012) in an attempt to refine the large spread in
66 values inferred from proxy data (from less than 900 ppm to over 5000 ppm). The typical atmospheric $p\text{CO}_2$
67 concentration resulting from these studies for the CT averages around a long-term value of 1120 ppm (Barron et
68 al., 1995; Bice and Norris, 2003; Royer, 2013; Wang et al., 2014), e.g., four times the
69 preindustrial value (280 ppm = 1 P.A.L. : “Preindustrial Atmospheric Level”). Atmospheric $p\text{CO}_2$ levels are
70 however, known to vary on shorter timescales during the period, in particular during OAE2. It has indeed been
71 suggested that this event may have been caused by a large increase in atmospheric $p\text{CO}_2$ concentration, possibly
72 reaching 2000 ppm or even higher, because of volcanic activity in large igneous provinces
73 (Kerr and Kerr, 1998; Turgeon and Creaser, 2008; Jenkyns, 2010). The proxy records suggest that
74 the $p\text{CO}_2$ levels may have dropped down to 900 ppm after carbon sequestration into organic-rich marine
75 sediments (Van Bentum et al., 2012).

76 Paleogeography is also considered as a major driver of climate change through geological times (Crowley
77 et al., 1986; Gyllenhaal et al., 1991; Goddérís et al., 2014; Lunt et al., 2016). Several processes linked to
78 paleogeographic changes have been shown to impact Cretaceous climates. These processes include albedo and
79 evapotranspiration feedbacks from paleovegetation (Otto-bliesner and Upchurch, 1997), seasonality due to
80 continental break-up or presence of epicontinental seas (Fluteau et al., 2007), atmospheric feedbacks due to
81 water cycle modification (Donnadieu et al., 2006), Walker and Hadley cells changes after Gondwana break-up
82 (Ohba and Ueda, 2011), or oceanic circulation changes due to gateways opening (Poulsen et al., 2001, 2003).
83 Other potential controlling factors include the time-varying solar constant (Gough, 1981), whose impact on
84 Cretaceous climate evolution was quantified by Lunt et al. (2016), and changes in the distribution of vegetation,
85 which has been suggested to drive warming, especially in the high-latitudes with a temperature increase of up to
86 $4^{\circ}\text{-}10^{\circ}\text{C}$ in polar regions (Otto-bliesner and Upchurch, 1997; Brady et al., 1998; Upchurch, 1998; Deconto et al.,
87 2000; Hunter et al., 2013).

88 Despite all these studies, there is no established consensus on the relative importance of each of
89 the controlling factors on the CT climate. In particular, the primary driver of the Cretaceous climate has been

90 suggested to be either $p\text{CO}_2$ or paleogeography. Early studies suggested a negligible role of paleogeography on
91 global climate compared to the high CO_2 concentration (Barron et al., 1995) whereas others suggested that CO_2
92 was not the primary control (Veizer et al., 2000) or that the impact of paleogeography on climate was as
93 important as a doubling of $p\text{CO}_2$ (Crowley et al., 1986). More recent modeling studies have also suggested that
94 paleogeographic changes could affect global climate (Poulsen et al., 2003; Donnadieu et al., 2006; Fluteau et al.,
95 2007) but their impact remain debated (Ladant and Donnadieu, 2016; Lunt et al., 2016; Tabor et al., 2016). For
96 example, the simulations of Lunt et al. (2016) support a key role of paleogeography at the
97 regional rather than global scale, and show that the global paleogeographic signal is cancelled by an opposite
98 trend due to changes in the solar constant. Tabor et al. (2016) also suggest important regional climatic
99 impacts of paleogeography, but argue that CO_2 is the main driver of the Late Cretaceous climate
100 evolution. In contrast, Ladant and Donnadieu (2016) find a large impact of paleogeography on
101 the global mean Late Cretaceous temperatures; their signal is roughly comparable to a doubling of atmospheric
102 $p\text{CO}_2$. Finally, the role of paleovegetation is also uncertain as some studies show a major role at high-latitude
103 (Upchurch, 1998; Hunter et al., 2013), whereas a more recent study instead suggests limited impact at high
104 latitudes ($<2^\circ\text{C}$) with a cooling effect at low latitudes under high $p\text{CO}_2$ values (Zhou et al., 2012).

105 In this study, we investigate the forcing parameters of CT greenhouse climate by using a set of
106 simulations run with the IPSL-CM5A2 Earth System Model. We perform six simulations, using both preindustrial
107 and CT boundary conditions, where we incrementally modify the preindustrial boundary conditions to that of the
108 CT. The changes are as follows: (1) the removal of polar ice sheets, (2) an increase in $p\text{CO}_2$ to 1120
109 ppm, (3) the change of vegetation and soil parameters to those found during the CT, (4) a 1% reduction in the
110 value of the solar constant, and (5) the implementation of Cenomanian-Turonian paleogeography. We
111 particularly focus on processes driving warming or cooling of atmospheric surface temperatures after each
112 change in boundary condition change to study the relative importance of each parameter in the CT to
113 preindustrial climate change. We also investigate how the SST gradient responds to boundary condition changes
114 to understand the evolution of its steepness between the CT and the preindustrial.

116 2. MODEL DESCRIPTION & EXPERIMENTAL DESIGN

117 2.1 IPSL-CM5A2 MODEL

118 IP SL-CM5A2 is an updated version of the IP SL-CM5A-LR earth system model developed at IP SL (Institut
119 Pierre-Simon Laplace) within the CMIP5 framework (Dufresne et al., 2013). It is a fully-coupled Earth
120 System Model, which simulates the interactions between atmosphere, ocean, sea ice, and land surface. The
121 model includes the marine carbon and other key biogeochemical cycles (C, P, N, O, Fe and Si - See Aumont et al.,
122 2015). Its former version, IP SL-CM5A-LR, has a rich history of applications, including present-day and future
123 climates (Aumont and Bopp, 2006; Swingedouw et al., 2017) as well as preindustrial (Gastineau et al., 2013) and
124 paleoclimate studies (Kageyama et al., 2013; Contoux et al., 2015; Bopp et al., 2017; Tan et al., 2017; Sarr et al.,
125 2019). It was also part of IPCC AR5 and CMIP5 projects (Dufresne et al., 2013),
126 . IP SL-CM5A-LR has also been used to explore links between marine productivity and climate (Bopp et al., 2013;
127 . IP SL-CM5A-LR has also been used to explore links between marine productivity
128 and climate (Bopp et al., 2013; Le Mézo et al., 2017; Ladant et al., 2018), vegetation and climate (Contoux et al.,
129 2013; Woillez et al., 2014), and topography and climate (Maffre et al., 2018), but also the role of nutrients in the
130 global carbon cycle (Tagliabue et al., 2010) or the variability of oceanic circulation and upwelling (Ortega et al.,
131 2015; Swingedouw et al., 2015). Building on recent technical developments, IP SL-CM5A2 provides enhanced
132 computing performances compared to IP SL-CM5A-LR, allowing thousand year-long integrations required for
133 deep-time paleoclimate applications or long-term future projections (Sepulchre et al., 2019). It thus
134 reasonably simulates modern-day and historical climates (despite some biases in the tropics), whose complete
135 description and evaluation can be found in Sepulchre et al., 2019.

136 IP SL-CM5A2 is composed of the LMDZ atmospheric model (Hourdin et al., 2013), the
137 ORCHIDEE land surface and vegetation model (including the continental hydrological cycle, vegetation, and
138 carbon cycle; Krinner et al., 2005) and the NEMO ocean model (Madec, 2012), including the LIM2 sea-ice
139 model (Fichefet and Maqueda, 1997) and the PISCES marine biogeochemistry model (Aumont et al., 2015). The
140 OASIS coupler (Valcke et al., 2006) ensures a good synchronization of the different components and the XIOS
141 input/output parallel library is used to read and write data. The LMDZ atmospheric component has a horizontal
142 resolution of 96x95, (equivalent to 3.75° in longitude and 1.875° in latitude) and 39 uneven vertical levels.
143 ORCHIDEE shares the same horizontal resolution whereas NEMO – the ocean component – has 31 uneven
144 vertical levels (from 10 meters at the surface to 500 meters at the bottom), and a horizontal resolution of
145 approximately 2°, enhanced to up to 0.5° in latitude in the tropics. NEMO uses the ORCA2.3 tripolar grid to
146 overcome the North Pole singularity (Madec and Imbard, 1996).

2.2 EXPERIMENTAL DESIGN

Six simulations were performed for this study: one preindustrial control simulation, named piControl, and five simulations for which the boundary conditions were changed one at a time to progressively reconstruct the CT climate (see Table 1 for details). The scenarios are called 1X-NOICE (with no polar ice caps), 4X-NOICE (no polar ice caps + pCO₂ at 1120 ppm), 4X-NOICE-PFT-SOIL (previous changes + implementation of idealized Plant Functional Types (PFTs) and mean parameters for soil), 4X-NOICE-PFT-SOIL-SOLAR (previous changes + reduction of the solar constant) and 4X-CRETACEOUS (previous changes + CT paleogeography). The piControl simulation has been run for 1800 years and the five others for 2000 years in order to reach near-surface equilibrium (see Fig.1).

2.2.1 BOUNDARY CONDITIONS

As most evidence suggests the absence of permanent polar ice sheets during the CT (MacLeod et al., 2013; Ladant and Donnadieu, 2016; Huber et al., 2018), we remove polar ice sheets in our simulations (except in piControl) and we adjust topography to account for isostatic rebound resulting from the loss of the land ice covering Greenland and Antarctica (See Supplementary Figure 1). Ice sheets are replaced with brown bare soil and the river routing stays unchanged.

In the 4X simulations (i.e., all except piControl and 1X-NOICE), pCO₂ is fixed to 1120 ppm (4x P.A.L), a value reasonably close to the mean suggested by a recent compilation of CT pCO₂ reconstructions (Wang et al., 2014).

In the 4X-NOICE-PFT-SOIL simulation, the distribution of the 13 standard PFTs defined in ORCHIDEE is uniformly reassigned along latitudinal bands, based on a rough comparison with the preindustrial distribution of vegetation, in order to obtain a theoretical latitudinal distribution usable for any geological period. The list of PFTs and associated latitudinal distribution and fractions are described in Supplementary Table 1. Mean soil parameters, i.e., mean soil color and texture (rugosity), are calculated from preindustrial maps (Zobler, 1999; Wilson and Henderson-sellers, 2003) and uniformly prescribed on all continents. The impact of these idealized PFTs and mean parameters is discussed in the results.

Commented [MG2]: Marie, I think this can be deleted You talk about the scenarios in detail below, and you will save some space and avoid repetition this way.

Commented [MG3]: If you do delete the above part, add here that « This scenario is referred to as 1X-NOICE in the following «

176 The 4X-NOICE-PFT-SOIL-SOLAR [simulation](#) is initialized from the same conditions as 4X-NOICE-PFT-SOIL
177 except that the solar constant is reduced to its CT value (Gough, 1981). We use here the value of 1353.36 W/m²
178 (98.9% of the modern solar luminosity, calculated for an age of 90 My).

179 The 4X-CRETACEOUS simulation, [finally](#), incorporates the previous modifications plus the implementation
180 of the CT paleogeography. The land-sea configuration used here is that proposed by Sewall (2007), in which we
181 have implemented the bathymetry from Müller (2008) ([see](#) Fig. 2). These bathymetric changes are done
182 to represent deep oceanic topographic features, such as ridges, that are absent from the Sewall paleogeographic
183 configuration. In this simulation, the mean soil color and rugosity as well as the theoretical latitudinal PFTs
184 distribution are adapted to the new land-sea mask and the river routing is recalculated from the new topography.
185 We [also](#) modify the [tidally driven mixing](#) associated with [dissipation o](#) internal wave energy
186 for the M2 and K1 tidal components [from present day values](#) (de Lavergne et al., 2019). The parameterization
187 used for simulations with the modern geography follows Simmons et al. (2004), with refinements in the modern
188 Indonesian Through Flow (ITF) region according to Koch-Larrouy et al. (2007). To create a Cenomanian-Turonian
189 [tidal](#) dissipation forcing, we calculate an M2 tidal dissipation field using the Oregon State University Tidal
190 Inversion System (OTIS, Egbert et al., 2004; Green and Huber, 2013). The M2 field is computed using our
191 Cenomanian-Turonian bathymetry and an ocean stratification taken from an unpublished equilibrated
192 Cenomanian-Turonian simulation realized with the IPSLCM5A2 with no M2 field. In the absence of any estimation
193 for the CT, we prescribe the K1 tidal dissipation field to 0. In addition, the parameterization of Koch-Larrouy et al.
194 (2007) is not used here because the ITF does not exist in the Cretaceous.

195 2.2.2 INITIAL CONDITIONS

197 The piControl and 1X-NOICE simulations are initialized with [conditions from the](#) Atmospheric Model
199 Intercomparison Project (AMIP) [which](#) were constrained by realistic sea surface temperature (SST)
200 and sea ice from 1979 to near present (Gates et al., 1999).

$$201 T = 10 + \left(\frac{1000 - depth}{1000} \right) * 25 \cos(latitude) \underline{\hspace{10em}} (1)$$

202

203 *Table 1 : Description of the simulations. The parameters in bold indicate the specific change for the corresponding simulation. Simulations are run for 2000 years, except piControl which is run*
 204 *for 1000 years.*

Simulation	piControl	1X-NOICE	4X-NOICE	4X-NOICE-PFT-SOIL	4X-NOICE-PFT-SOIL-SOLAR	4X-CRETACEOUS
Polar Caps	Yes	No	No	No	No	No
CO ₂ (ppm)	280	280	1120	1120	1120	1120
Vegetation	IPCC (1850)	IPCC (1850) + Bare soil instead of polar caps	IPCC (1850) + Bare soil instead of polar caps	Theoretical latitudinal PFTs	Theoretical latitudinal PFTs	Theoretical latitudinal PFTs
Soil Color/Texture	IPCC (1850)	IPCC (1850) + Brown soil instead of polar caps	IPCC (1850) + Brown soil instead of polar caps	Uniform mean value	Uniform mean value	Uniform mean value
Solar constant (W/m ²)	1365.6537	1365.6537	1365.6537	1365.6537	1353.36	1353.36
Geographic configuration	Modern	Modern	Modern	Modern	Modern	Cretaceous 90 Ma (Sewall 2007 + Müller 2008)

205

206 3. RESULTS

207 The simulated changes between the preindustrial (piControl) and the CT (4X-CRETACEOUS)
208 simulations can be decomposed into five components based on our boundary condition changes: (1)
209 Polar ice sheet removal (Δ_{ice}), (2) pCO_2 (Δ_{CO_2}), (3) PFT and Soil parameters ($\Delta_{PFT-SOIL}$), (4) Solar
210 constant (Δ_{solar}) and (5) Paleogeography (Δ_{paleo}). Each contribution to the total climate change can
211 be calculated by a linear factorization (Broccoli and Manabe, 1987; Von Deimling et al., 2006), which
212 simply corresponds to the anomaly between two consecutive simulations. The choice of applying a
213 linear factorization approach was made for due to problems of computing time and cost. Changing the
214 sequence of changes or applying a symmetrical factorization as in Lunt et al (2012b) would require too
215 many supplementary simulations; ~~Such at these~~ methods ~~is dependent~~ depend on the sequence of
216 changes, and the intensity of simulated warming/cooling for each component could differ if boundary
217 conditions were changed in a different order (Lunt et al., 2012b), and the costs would be too high for
218 this study. The results presented in the following are averages calculated over the last 100 simulated
219 years.

221 3.1 GLOBAL CHANGES

222 The progressive change of parameters made to reconstruct the CT climate induces a general
223 global warming (Table 2, Fig. 3). The annual global atmospheric ice temperature at 2 meters above the
224 surface (T2M) rises from 13.25°C to 24.35 °C between the preindustrial and CT simulations. Every-All
225 changes in boundary conditions generates a warming signal at the on a global scale, at with the
226 exception of the decrease in solar constant that which generates a cooling. Most of the warming is
227 due to the fourfold increase in atmospheric pCO_2 , which alone increases the global mean
228 temperature by 9°C. Paleogeographic changes also represent a major contributor to the warming,
229 leading to an increase in T2M of 2.6°C. In contrast, the decrease in solar constant leads to a cooling of
230 1.8°C at the global scale. Finally, changes in the soil parameters and PFTs, as well as the retreat of
231 polar caps, have smaller impacts, leading to increases in global mean T2M of 0.8°C and 0.5°C
232 respectively.

233 Temperature changes exhibit different geographic patterns (Fig. 4) depending on the
234 altered which parameter is changed. These patterns range from global and uniform cooling (Δ_{solar} –
235 Fig 4e) to a global, polar-amplified, warming (Δ_{pCO_2} – Fig 4c), as well as heterogeneous regional
236 responses (Δ_{ice} or Δ_{paleo} – Fig 4b and 4f). In the next section, we describe the main patterns of
237 change and the main feedbacks arising.

238

Commented [MG4]: How about this is changed to

The choice of applying a linear factorization approach was made due to computing time and cost. We appreciate that another sequence of changes could lead to a different final state, but as we show in section 4, our results are within the ranges provided by existing proxies for the CT. The computational costs would be too high for this study to explore this further here; it is an interesting problem that we leave for a future investigation.

	piControl	1X-NOICE	4X-NOICE	4X-NOICE- PFT-SOIL	4X-NOICE- PFT-SOIL- SOLAR	4X- CRETACEOUS
T2M (°C)	13.25	13.75	22.75	23.55	21.75	24.35
Planetary Albedo (%)	33.1	32.6	28.8	28.3	28.7	27.1
Surface Albedo (%)	20.1	19	16.6	15.5	15.3	14.9
Emissivity (%)	62	61.7	57.5	57.1	57.8	57

Table 2: Simulations results (Global annual mean over last 100 years of simulation).

240

241

242 3.2 The major contributor to global warming - ΔCO_2

243 [As mentioned above](#), the fourfold increase in $p\text{CO}_2$ leads to a global warming of 9°C (Table 3,
 244 Fig. 3) between [the 1X-NOICE](#) and [the 4X-NOICE](#) simulations. The whole Earth warms, with an
 245 amplification located over the Arctic and Austral oceans and a warming generally larger over
 246 continents than over oceans (Fig 4c). The warming is due to a general decrease of planetary albedo
 247 and of the atmosphere's emissivity (see Supplementary Figure 2). The decrease in [the](#) atmosphere's
 248 emissivity is directly driven by the increase in CO_2 , and thus greenhouse trapping in the atmosphere. It
 249 is also amplified by an increase in high-altitude cloudiness (defined as cloudiness at atmospheric
 250 pressure < 440 hPa) over the Antarctic continent (Fig 5a, b). The decrease in planetary albedo is due to
 251 two major processes. First, a decrease of sea ice and snow cover (especially over Northern
 252 Hemisphere continents and along the coasts of Antarctica), leading to surface albedo decrease,
 253 explains the warming amplification over polar oceans and continents. Second, a decrease in low-
 254 altitude cloudiness (defined as cloudiness at atmospheric pressure > 680 hPa) at all latitudes except
 255 over the Arctic (Fig 5a, b) leads to an increase in absorbed solar radiation.

256 The contrast in the atmospheric response over continents and oceans is due to the impact of
 257 the evapo-transpiration feedback. Oceanic warming drives an increase in evaporation, which acts as a
 258 negative feedback and moderates the warming by consuming more latent heat at the ocean surface.
 259 In contrast, high temperatures resulting from continental warming tend to inhibit vegetation
 260 development, which acts as positive feedback and enhances the warming due to reduced
 261 transpiration and reduced latent heat consumption.

262

263 3.3 Boundary conditions with the smallest global impacts – Δice , $\Delta\text{PFT-SOIL}$, Δsolar

264 The removal of polar ice sheets in the 1X-NOICE simulation leads to a weak global warming of
 265 0.5°C but a strong regional warming observed over areas previously covered by the Antarctic and
 266 Greenland ice sheets (Fig 4a, b). This signal is due to the combination of a decrease in elevation ([i.e.](#),

267 lapse rate feedback – Supplementary Figure S3) and in surface albedo, which is directly linked to the
268 shift from a reflective ice surface to a darker bare soil surface. Unexpected cooling is also simulated in
269 specific areas, such as the margins of the Arctic Ocean and the southwestern Pacific. These contrasted
270 climatic responses to the impact of ice sheets on sea surface temperatures are consistent with
271 previous modeling studies (Goldner et al., 2014; Knorr and Lohmann, 2014; Kennedy et al., 2015).
272 Their origin is still unclear but changes in winds in the Southern Ocean, due to topographic changes
273 after polar ice sheet removal, may locally impact oceanic currents, deep-water formation, and thus
274 oceanic heat transport and temperature distribution. In the Northern Hemisphere, the observed
275 cooling over Eurasia could be linked to stationary wave feedbacks following changes in topography
276 after Greenland ice sheet removal (Supplementary Figure S4; see also Maffre et al., 2018).

277 The change in soil parameters and the implementation of theoretical zonal PFTs in the 4X-
278 NOICE-PFT-SOIL simulation drive a warming of 0.8 °C. This warming is essentially located above arid
279 areas, such as the Sahara, Australia, or Middle East, and polar latitudes (Antarctica/Greenland) (Fig
280 4d), and is mostly caused by the implementation of a mean uniform soil color, which drives a surface
281 albedo decrease over deserts that normally have a lighter color. The warming at high-latitudes is
282 linked to vegetation change: bare soil that characterizes continental regions previously covered with
283 ice is replaced by boreal vegetation with a lower surface albedo. The presence of vegetation at such
284 high-latitudes is consistent with high-latitude paleobotanical data and temperature records during the
285 Cretaceous (Otto-bliesner and Upchurch, 1997; Herman and Spicer, 2010; Spicer and Herman, 2010).

286 Finally, the change in solar constant from 1365 W/m² to 1353 W/m² (Gough 1981) directly
287 drives a cooling of 1.8 °C evenly distributed over the [planet](#) (Fig 4e).

288

289 3.4 The most complex response - Δpaleogeography

290 The paleogeographic change drives a global warming of 2.6 °C. This is seen year-round in the
291 Southern Hemisphere, while the Northern Hemisphere experiences [a](#) warming during winter and
292 cooling during summer [compared to pre-industrial conditions](#) (Fig 6). These temperature changes are
293 linked to a general decrease in planetary albedo and/or emissivity, although the Northern Hemisphere
294 sometimes exhibits increased albedo, due to the increase in low-altitude cloudiness. This increase in
295 albedo is compensated by a strong atmosphere emissivity decrease during winter but not during
296 summer, which leads to the seasonal pattern of cooling and warming (Supplementary Figure S5).

297 The albedo and emissivity changes are linked to atmospheric and oceanic circulation
298 modifications driven by [four](#) major features of the CT paleogeography (Fig 2):

- 299 (1) Equatorial oceanic gateway opening (Central American Seaway/Neotethys)
- 300 (2) Polar gateway closure (Drake/Tasman)

- 301 (3) Increase in oceanic area in the North Hemisphere (Fig 2)
302 (4) Decrease in oceanic area in the South Hemisphere (Fig 2)

303
304 In the CT simulation, we observe an intensification of the meridional surface circulation and
305 extension towards higher latitudes compared to the simulation with the modern geography (Fig8a-b),
306 as well as an intensification of subtropical gyres, especially in the Pacific (Supplementary Figure S6),
307 which are responsible for an increase in poleward oceanic heat transport (OHT – Fig 8c). Such
308 modifications can be linked to the opening of equatorial gateways that creates a zonal connection
309 between the Pacific, Atlantic and Neotethys oceans (Enderton and Marshall, 2008; Hotinski and
310 Toggweiler, 2003) and that leads to the formation of a strong circumglobal equatorial current (Fig 7b) .
311 This connection permits the existence of stronger easterly winds that enhance equatorial upwelling
312 and drive increased export of water and heat from low latitudes to polar regions. In the Southern
313 Hemisphere, the Drake Passage is only open to shallow flow, and the Tasman gateway has not yet
314 formed. The closure of these zonal connections leads to the disappearance of the modern Antarctic
315 Circumpolar Current (ACC) during the Cretaceous (Fig 7c-d). Notwithstanding, the observed increase
316 in southward OHT between 40° and 60°S (Fig 8c) is explained by the absence of significant zonal
317 connections in the Southern Ocean, which allows for the buildup of polar gyres in the CT simulation
318 (Supplementary Figure S6).

319 The increase in OHT is associated with a meridional expansion of high sea-surface
320 temperatures leading to an intensification of evaporation between the tropics and a poleward shift of
321 the ascending branches of the Hadley cells. The combination of these two processes results in a
322 greater injection of moisture into the atmosphere between the tropics (Supplementary Figure S7).
323 Consequently, the high-altitude cloudiness increases and spreads towards the tropics, leading to
324 an enhanced greenhouse effect. This process is the main driver of the
325 intertropical warming (Herweijer et al., 2005; Levine and Schneider, 2010; Rose and Ferreira, 2013).

326 The atmosphere's response to the paleogeographic changes in the mid- and high-latitudes is
327 different in the Southern and Northern Hemispheres because the ocean to land ratio
328 varies between the CT configuration and the modern. In the Southern Hemisphere, the reduced ocean
329 surface area (Fig 2) limits evaporation and moisture injection into the atmosphere, which in turn leads
330 to a decrease in relative humidity and low-altitude cloudiness (Supplementary Fig S8) and associated
331 year-round warming due to reduced planetary albedo. In the Northern Hemisphere, oceanic surface
332 area increases (Fig 2) and results in a strong increase in evaporation and moisture injection into the
333 atmosphere. Low-altitude cloudiness and planetary albedo increase and lead to summer cooling, as
334 discussed above (Fig 6). During winter an increase in high-altitude cloudiness leads to an enhanced
335 greenhouse effect and counteracts the larger albedo. This high-altitude cloudiness increase is

Commented [MG5]: in the CT simulation ? please specify

336 consistent with the simulated increase in extratropical OHT (Fig. 8). Mid-latitude convection and moist
337 air injection into the upper troposphere is consequently enhanced and efficiently transported
338 poleward (Rose and Ferreira, 2013; Ladant and Donnadieu, 2016). In addition, increased continental
339 fragmentation in the CT paleogeography relative to the preindustrial decreases the effect of
340 continentality (Donnadieu et al. 2006) because thermal inertia is greater in the ocean than over
341 continents.

342

343 3.5 Temperature Gradients

344 3.5.1 Ocean

345 The mean annual global SST increases as much as 9.8°C (from 17.9°C to 27.7 °C) across the
346 simulations. The SST warming is slightly weaker than that of the mean annual global
347 atmospheric temperature at 2m discussed above, and most likely occurs because of evaporation
348 processes due to the weaker atmospheric warming simulated above oceans compared to that
349 simulated above continents. Unsurprisingly, as for the atmospheric temperatures, $p\text{CO}_2$
350 is the major controlling parameter of the ocean warming (7°C), followed by paleogeography
351 (4.5°C) and changes in the solar constant (2.3°C), although the latter induces a cooling rather
352 than a warming. PFT and soil parameter changes and the removal of polar ice sheets have a minor
353 impact at the global SST (0.6 °C and 0°C respectively). It is interesting to note the increased
354 contribution of paleogeography to the simulated SST warming compared to its contribution to the
355 simulated atmospheric warming, which is probably driven by the major changes simulated in surface
356 ocean circulation (Fig. 7).

357 Mean annual SST in the preindustrial simulation reach ~ 26°C in the tropics (calculated as the
358 zonal average between 30°S and 30°N) and ~ -1.5°C at the poles (beyond 70° N - Fig 9a). In this work,
359 we define the meridional temperature gradients as the linear temperature change per 1° of latitude
360 between 30° and 80°. The gradients in the piControl experiment then amount to
361 0.45°C/°latitude and 0.44°C/°latitude for the Northern and Southern Hemispheres, respectively. In the
362 CT simulation, the mean annual SST reach ~ 33.3°C in the tropics, and ~5°C and 10°C in the Arctic and
363 Southern Ocean respectively, and the simulated CT meridional gradients are 0.45°C/°latitude and
364 0.39°C/°latitude for the Northern and Southern Hemispheres, respectively.

365 The progressive flattening of the SST gradient can be visualized by superimposing the zonal
366 mean temperatures of the different simulations and by adjusting them at the Equator (Fig 9b). Two
367 major observations can be drawn from these results. First, paleogeography has a strong impact on the
368 low-latitudes (< 30° of latitude) SST gradient because it widens the latitudinal band of relatively
369 homogeneous warm tropical SST as a result of the opening of equatorial gateways. Second, poleward

370 of 40° [in](#) latitude, the paleogeography and the increase in atmospheric pCO₂ both contribute to the
371 flattening of the SST gradient with a larger influence from paleogeography than from atmospheric
372 pCO₂.

373

374 3.5.2 Atmosphere

375 In the preindustrial simulation, mean tropical atmospheric temperatures reach ~ 23.6°C
376 whereas polar temperatures (calculated as the average between 80° and 90° of latitude) in the
377 Northern and Southern Hemispheres reach around -16.8°C and -37°C respectively. The northern
378 meridional temperature gradient is 0.69°C/°latitude while the southern latitudinal temperature
379 gradient is 1.07°C/°latitude (Fig 9c). This significant difference is explained by the very negative mean
380 annual temperatures over Antarctica linked to the presence of the ice sheet.

381 In the CT simulation, mean tropical atmospheric temperatures reach ~ 32.3°C whereas polar
382 temperatures reach ~ 3.4°C in the Northern Hemisphere and ~ -0.5°C in the Southern Hemisphere,
383 thereby yielding latitudinal temperature gradients of 0.49°C/°latitude and 0.54°C/°latitude,
384 respectively. [The gradients](#) are reduced compared to the preindustrial because the absence
385 of year-round sea and land ice at the poles drives [leads to far](#) higher polar temperatures.

386 As for [the](#) SST gradients, we plot atmospheric meridional gradients by adjusting
387 temperature values so that temperatures at the Equator are equal for each simulation (Fig 9d). This
388 normalization reveals that the mechanisms responsible for the flattening of the gradients are different
389 for each hemisphere. In the Southern Hemisphere high-latitudes (> 60° of latitude), three parameters
390 contribute to reducing the equator-to-pole temperature gradient in the following order of
391 importance: removal of polar ice sheets, paleogeography and increase in atmospheric pCO₂. In
392 contrast, the reduction in the gradient steepness in the Northern Hemisphere high-latitudes is
393 exclusively explained by the increase in atmospheric pCO₂. In the low- and mid-latitudes, this
394 temperature gradient reduction is essentially explained by paleogeography in the Southern
395 Hemisphere and by a similar contribution of paleogeographic changes and increase in atmospheric
396 pCO₂ in the Northern Hemisphere.

397 4. DISCUSSION

398

399 4.1 CENOMANIAN-TURONIAN MODEL/DATA COMPARISON

400 The results predicted by our CT simulation [can be](#) compared to reconstructions of
401 atmospheric and oceanic paleotemperatures inferred from proxy data (Fig 10a, b). Our SST data
402 compilation is [a modified version of](#) Tabor et al (2016), with additional data from more recent
403 studies ([see our](#) Supplementary data). We also compiled atmospheric temperature data obtained

404 from paleobotanical and paleosoil studies (see Supplementary data for the complete database and
405 references).

406 [The](#) Cretaceous equatorial and tropical SST have long been believed to be similar or even
407 lower than those of today (Sellwood et al., 1994; Crowley and Zachos, 1999; Huber et al., 2002), thus
408 feeding the problem of “tropical overheating” systematically observed in General Circulation Model
409 simulations (Barron et al., 1995; Bush et al., 1997; Poulsen et al., 1998). This incongruence was based
410 on the relatively low tropical temperatures reconstructed from foraminiferal calcite (25-30°C, Fig. 9a),
411 but subsequent work suggested that these were underestimated because of diagenetic alteration
412 (Pearson et al., 2001; Pucéat et al., 2007). Latest data compilations including temperature
413 reconstructions from other proxies, such as TEX86, have provided support for high tropical SST in the
414 Cenomanian-Turonian (Tabor et al., 2016; O’Brien et al., 2017) and our tropical SST are mostly
415 consistent with existing paleotemperature reconstructions (Fig. 10a). In the mid-latitudes (30-60°),
416 proxy records infer a wide range of possible SST, ranging from 10°C to more than 30°C. Simulated
417 temperatures in our CT simulation reasonably agree with these reconstructions if seasonal variability,
418 represented by local monthly maximum and minimum temperatures (grey shaded areas, Fig 10a), is
419 considered. This congruence would imply that a seasonal bias may exist in temperatures
420 reconstructed from proxies, which is suggested in previous studies (Sluijs et al., 2006; Hollis et al.,
421 2012; Huber, 2012; Steinig et al., 2020) but still debated (Tierney, 2012). There are unfortunately only
422 a few high-latitudes SST data points available, which render the model-data comparison difficult. In
423 the Northern Hemisphere, the presence of crocodilian fossils (Vandermark et al., 2007) in the
424 northern Labrador Sea (~70° of latitude) imply mean annual temperature of at least 14°C and
425 temperature of the coldest month of at least 5°C. In comparison, simulated temperatures at the same
426 latitude in the adjacent Western Interior Sea are very similar (13.5 °C for the annual mean and 7.9 °C
427 for the coldest month). In the Southern Hemisphere, mean annual SST calculated from foraminiferal
428 calcite at DSDP sites 511 and 258 are between 25° and 28°C (Huber et al., 2018). Simulated annual SST
429 reach a monthly maximum of 28°C around the location of site DSDP 258. We speculate that a seasonal
430 bias in the foraminiferal record may represent a possible cause for this difference; alternatively, local
431 deviations of the regional seawater $\delta^{18}\text{O}$ from the globally assumed -1‰ value may also reduce the
432 model-data discrepancy (Zhou et al., 2008; Zhu et al., 2020).

433 To our knowledge, atmospheric temperature reconstructions from tropical latitudes are
434 [not available](#). In the mid-latitudes (30-60°), simulated atmospheric temperatures in the
435 Southern Hemisphere reveal reasonable agreement with data whereas Northern Hemisphere mean
436 zonal temperatures in our model are slightly warmer than that inferred from proxies (Fig 10b). At
437 high-latitudes, the same trend is observed for atmospheric temperatures as it is for SST with data
438 indicating higher temperatures than the model in both the Southern and Northern Hemispheres. This

439 inter-hemispheric symmetry in model-data discrepancy could indicate a systematic cool bias of the
440 simulated temperatures.

441 4.2 RECONSTRUCTED LATITUDINAL TEMPERATURE GRADIENTS

442 The simulated northern hemisphere latitudinal SST gradient of ($\sim 0.45^{\circ}\text{C}/^{\circ}\text{latitude}$) is in good
443 agreement with those reconstructed from paleoceanographic data in the Northern Hemisphere
444 ($\sim 0.42^{\circ}\text{C}/^{\circ}\text{latitude}$) whereas it is much larger in the Southern Hemisphere
445 ($\sim 0.39^{\circ}\text{C}/^{\circ}\text{latitude}$ vs $\sim 0.3^{\circ}\text{C}/^{\circ}\text{latitude}$) (Fig 11). This overestimate of the latitudinal gradient holds
446 for the atmosphere as well, as gradients inferred from data are much lower (North= $0.2^{\circ}\text{C}/^{\circ}\text{latitude}$
447 and South= $0.18^{\circ}\text{C}/^{\circ}\text{latitude}$) than simulated gradients (North= $0.49^{\circ}\text{C}/^{\circ}\text{latitude}$ and
448 South= $0.55^{\circ}\text{C}/^{\circ}\text{latitude}$), although the paucity of Cenomanian-Turonian continental temperatures
449 proxy data is likely to significantly bias this comparison.

450 In the following, we compare our simulated gradients to those obtained in previous deep time
451 modelling studies using recent earth system models. Because Earth system models studies focusing
452 on the Cenomanian-Turonian are limited in numbers, we include simulations of the Early Eocene (~ 55
453 Ma), which is another interval of global climatic warmth (Lunt et al., 2012a, 2017) (Fig. 11). The
454 simulated SST latitudinal gradients range from $0.32^{\circ}\text{C}/^{\circ}\text{latitude}$ to $0.55^{\circ}\text{C}/^{\circ}\text{latitude}$ (Lunt et al., 2012;
455 Tabor et al., 2016; Zhu et al., 2019; Fig. 11) and the atmospheric latitudinal gradients from
456 $0.33^{\circ}\text{C}/^{\circ}\text{latitude}$ to $0.78^{\circ}\text{C}/^{\circ}\text{latitude}$ (Huber and Caballero, 2011; Lunt et al., 2012; Niezgodzki et al.,
457 2017; Upchurch et al., 2015; Zhu et al., 2019; Fig. 11). For a single model and a single set of boundary
458 conditions (Cretaceous or Eocene), the lowest latitudinal gradient is obtained for the highest $p\text{CO}_2$
459 value. However, when comparing different studies with the same model (Cretaceous vs Eocene
460 using the ECHAM5 model; REF) it is not the case: the South Hemisphere atmospheric gradient
461 obtained for the Eocene with the ECHAM5 model is always lower than those obtained for the
462 Cretaceous with the same model, regardless of the $p\text{CO}_2$ value (Fig. 11 and Supplementary Data).
463 These results show the major role of boundary conditions (in particular paleogeography) in defining
464 the latitudinal temperature gradient. IPSL-CM5A2 predicts SST and atmosphere gradients that are well
465 within the range of other models of comparable resolution and complexity. Models almost
466 systematically simulate larger gradients than those obtained from data (Fig. 11, see also Huber, 2012).
467 The reasons behind this incongruence are debated (Huber, 2012) but highlight the need for
468 more data and for challenging the behavior of complex earth system models, in particular in the high
469 latitudes. Studies have demonstrated that models are able to simulate lower latitudinal temperature
470 gradients under specific conditions such as anomalously high CO_2 concentrations (Huber and
471 Caballero, 2011), modified cloud properties and radiative parameterizations (Upchurch et al., 2015;
472 Zhu et al., 2019) or lower paleo elevations and/or more extensive wetlands (Hay et al., 2019). Finally,

Commented [MG6]: you need a reference here

473 from a proxy perspective, it has been suggested that a sampling bias could exist, with a better record
474 of temperatures during the warm season at high latitudes and during the cold season in low latitudes
475 (Huber, 2012). Such possible biases would help reduce the model-data discrepancy, in particular for
476 atmospheric temperatures (Fig 10b), as high-latitude reconstructed temperatures are more consistent
477 with simulated summer temperatures whereas the consistency is better with simulated winter
478 temperatures in the mid- to low-latitudes, but further work is required to unambiguously demonstrate
479 the existence of these biases.

480

481 4.3 PRIMARY CLIMATE CONTROLS

482

483 The earliest estimates of climate sensitivity (or the temperature change under a doubling of
484 the atmospheric $p\text{CO}_2$) predicted a 1.5 to 4.5°C temperature increase, with the most likely scenario
485 [providing an increase of 2.5°C](#) (Charney et al., 1979; Barron et al., 1995; Sellers et al., 1996;
486 IPCC, 2014). Our modelling study predicts an atmospheric warming of 11.1°C for the CT. The signal is
487 notably due to a 9°C warming in response to the fourfold increase in $p\text{CO}_2$, which converts to an
488 increase of 4.5°C for a doubling of $p\text{CO}_2$ (assuming a linear response). This climate sensitivity agrees
489 with the higher end of the range of previous estimates (+ add references again). However, our
490 simulated climate sensitivity could be slightly lower as the simulations are not completely equilibrated
491 (Fig. 1). The latest generation of Earth system models used in deep-time paleoclimate also show an
492 increasingly higher climate sensitivity to increased CO_2 (Hutchinson et al., 2018; Golaz et al., 2019; Zhu
493 et al., 2019), suggesting that the sensitivity could have been underestimated in earlier studies. For
494 example, the recent study of Zhu (2019), using an up-to-date parameterization of cloud microphysics
495 in the CESM1.2 model, proposes an Eocene Climate Sensitivity of 6.6°C for a doubling of CO_2 from 3 to
496 6 PAL.

497 We have shown that $p\text{CO}_2$ is the main controlling factor for atmospheric global warming
498 whereas the effects of the paleogeography (warming) and reduced solar constant (cooling) nearly
499 cancel each other out at the global scale (see also Lunt et al., 2016). These results agree with previous
500 studies suggesting that $p\text{CO}_2$ is the main factor controlling climate (Barron et al., 1995; Crowley and
501 Berner, 2001; Royer et al., 2007; Foster et al., 2017). However, we also demonstrate that
502 paleogeography plays a major role in the latitudinal distribution of temperatures and impacts oceanic
503 temperatures (with a similar magnitude than a doubling of $p\text{CO}_2$), thus confirming that it is also a
504 critical driver of the Earth's climate (Poulsen et al., 2003; Donnadieu et al., 2006; Fluteau et al., 2007;
505 Lunt et al., 2016). The large climatic influence of the continental configuration has not been reported
506 for paleogeographic configurations closer to each other, e.g., the Maastrichtian and Cenomanian
507 (Tabor et al., 2016). The main features influencing climate in our study (i.e. the configuration of

Commented [MG7]: dont forget to do this !

508 equatorial and polar zonal connections and the land/sea distribution) are indeed not fundamentally
509 different in the two geological periods investigated by Tabor et al. (2016). Paleogeography is thus a
510 first-order control on climate over long timescales.

511 Early work has suggested that high latitude warming can be amplified in deep time simulations
512 by rising CO₂ via cloud and vegetation feedbacks (Otto-bliesner and Upchurch, 1997; Deconto et al.,
513 2000) or by increasing ocean heat transport (Barron et al., 1995; Schmidt and Mysak, 1996; Brady et
514 al., 1998), in particular when changing the paleogeography (Hotinski and Toggweiler, 2003). Our study
515 confirms that the paleogeography is a primary control on the steepness of the oceanic meridional
516 temperature gradient. Furthermore, paleogeography is the only process, among those investigated,
517 that controls both the atmosphere and ocean temperature gradients in the tropics and it
518 has a greater impact than atmospheric CO₂ on the reduction of the
519 atmospheric temperature gradient at high latitudes in the Southern Hemisphere between the CT and
520 the preindustrial. The increase in *p*CO₂ appears as the second most important parameter controlling
521 the SST gradient at high latitudes and is the main control of the reduced atmospheric gradient in the
522 Northern Hemisphere due to low cloud albedo feedback. The effect of paleovegetation on the
523 reduced temperature gradient is marginal at high latitudes in our simulations, in contrast to the
524 significant warming reported in early studies (Otto-bliesner and Upchurch, 1997; Upchurch, 1998;
525 Deconto et al., 2000) but in agreement with more recent model simulations suggesting a limited
526 influence of vegetation in the Cretaceous high-latitudes warmth (Zhou et al., 2012). However, our
527 modeling setup prescribes boreal vegetation at latitudes higher than 50° whereas evidence exist to
528 support the development of evergreen forests poleward of 60° of latitude (Sewall et al., 2007; Hay et
529 al., 2019) and of temperate forests up to 60° of latitude (Otto-bliesner and Upchurch, 1997). The
530 presence of such vegetation types could change the albedo of continental regions but also heat and
531 water vapor transfer by altered evapo-transpiration processes, thus leading to warming amplification
532 at high-latitudes and reduced temperature gradients (Otto-bliesner and Upchurch, 1997; Hay et al.,
533 2019). Based on these studies and on our results, we cannot exclude that different types of high-
534 latitude could promote a greater impact of paleovegetation in reducing the temperature gradient.

535

536 5. CONCLUSIONS

537 To quantify the impact of major climate forcings on the Cenomanian-Turonian climate, we
538 perform a series of 6 simulations using the IPSL-CM5A2 earth system model in which we incrementally
539 implement changes in boundary conditions on a preindustrial simulation to obtain ultimately a
540 simulation of the Cenomanian-Turonian stage of the Cretaceous. This study confirms the primary
541 control exerted by atmospheric *p*CO₂ on atmospheric and sea-surface temperatures, followed by

542 paleogeography. In contrast, the flattening of meridional SST gradients between the preindustrial and
543 the CT is mainly due to paleogeographic changes and to a lesser extent to the increase in $p\text{CO}_2$. The
544 atmospheric gradient response is more complex because the flattening is controlled by several factors
545 including paleogeography, $p\text{CO}_2$ and polar ice sheet retreat. While predicted oceanic and atmospheric
546 temperatures show reasonable agreement with data in the low and mid latitudes, predicted
547 temperatures in the high latitudes are colder than paleotemperatures reconstructed from proxies,
548 which leads to steeper equator-to-pole gradients in the model than [those](#) inferred from proxies.
549 However, this mismatch, often observed in data-model comparison studies, has been reduced in the
550 last decades and could be further resolved by considering possible sampling/seasonal biases in the
551 proxies and by continuously improving model physics and parameterizations.
552

553 DATA AVAILABILITY

554 Code availability:

555 LMDZ, XIOS, NEMO and ORCHIDEE are released under the terms of the CeCILL license. OASIS-MCT is
556 released under the terms of the Lesser GNU General Public License (LGPL). IPSL-CM5A2 code is
557 publicly available through svn, with the following command lines: `svn co`
558 `http://forge.ipsl.jussieu.fr/igcmg/svn/modipsl/branches/publications/IPSLCM5A2.1_11192019`
559 `modipsl`

560 `cd modipsl/util;./model IPSLCM5A2.1`

561 The mod.def file provides information regarding the different revisions used, namely :

- 562 – NEMOGCM branch nemo_v3_6_STABLE revision 6665
- 563 – XIOS2 branches/xios-2.5 revision 1763
- 564 – IOIPSL/src svn tags/v2_2_2
- 565 – LMDZ5 branches/IPSLCM5A2.1 rev 3591
- 566 – branches/publications/ORCHIDEE_IPSLCM5A2.1.r5307 rev 6336
- 567 – OASIS3-MCT 2.0_branch (rev 4775 IPSL server)

568 The login/password combination requested at first use to download the ORCHIDEE component is
569 anonymous/anonymous. We recommend to refer to the project website:

570 `http://forge.ipsl.jussieu.fr/igcmg_doc/wiki/Doc/Config/IPSLCM5A2` for a proper installation and
571 compilation of the environment.

572

573 Data availability: Data that support the results of this study, as well as boundary condition files are
574 available on request to the authors.

575 AUTHOR CONTRIBUTION

576 M.L performed and analyzed the numerical simulations, in close cooperation with Y.D and J.B.L, and
577 led the writing. M.G run the OTIS model to provide the Cenomanian-Turonian [tidal](#)
578 [dissipation](#). All authors discussed the results and analyses presented in the final version of
579 the manuscript.

580 COMPETING INTERESTS

581 The authors declare that they do not have competing interests.

582 ACKNOWLEDGMENTS

583 We express our thanks to Total E&P for funding the project and granting permission to publish. We
584 thank the CEA/CCRT for providing access to the HPC resources of TGCC under the allocation 2018-
585 GEN2212 made by GENCI. J.A.M.G receives funding from the Natural Environmental Research Council
586 (grant NE/S009566/1, MATCH). We acknowledge use of the Ferret (ferret.pmel.noaa.gov/Ferret/)
587 program for analysis and graphics in this paper.

588 FIGURES

589

Figure 1: Time series for mean annual oceanic temperatures. (a) Sea-surface temperature and (b) deep-ocean (2500 m) temperature. The piControl and 1X-NOICE simulations are perfectly equilibrated. The 4X simulations still have a small linear drift, around 0.1°C/century or less : 0.07, 0.08, 0.05 and 0.01°C/century during the last 500 years for SST of 4X-NOICE, 4X-NOICE-PFT-SOIL, 4X-NOICE-PFT-SOIL-SOLAR and 4X-CRETACEOUS respectively; 0.11, 0.08, 0.07 and 0.06°C/century during the last 500 years, for deep-ocean of 4X-NOICE, 4X-NOICE-PFT-SOIL, 4X-NOICE-PFT-SOIL-SOLAR and 4X-CRETACEOUS respectively.

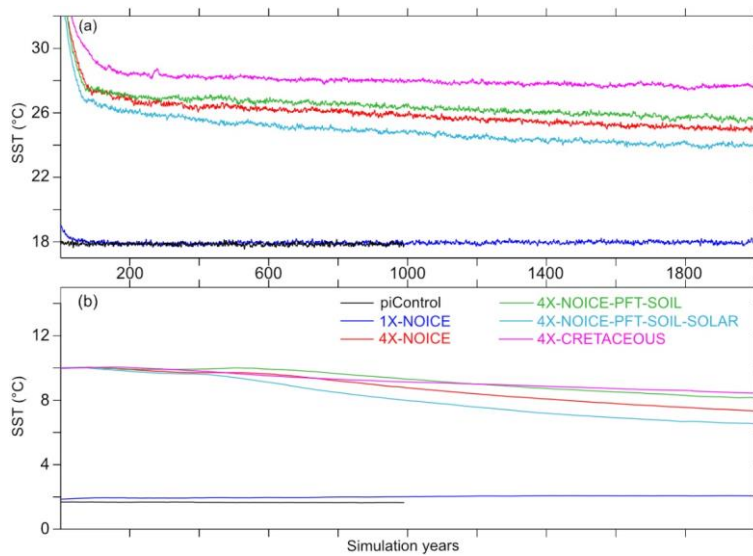


Figure 2: Modern and Cenomanian-Turonian geographic configurations used for the piControl and 4X-CRETACEOUS simulations respectively, and meridional oceanic area anomaly between Cretaceous paleogeography and Modern geography.

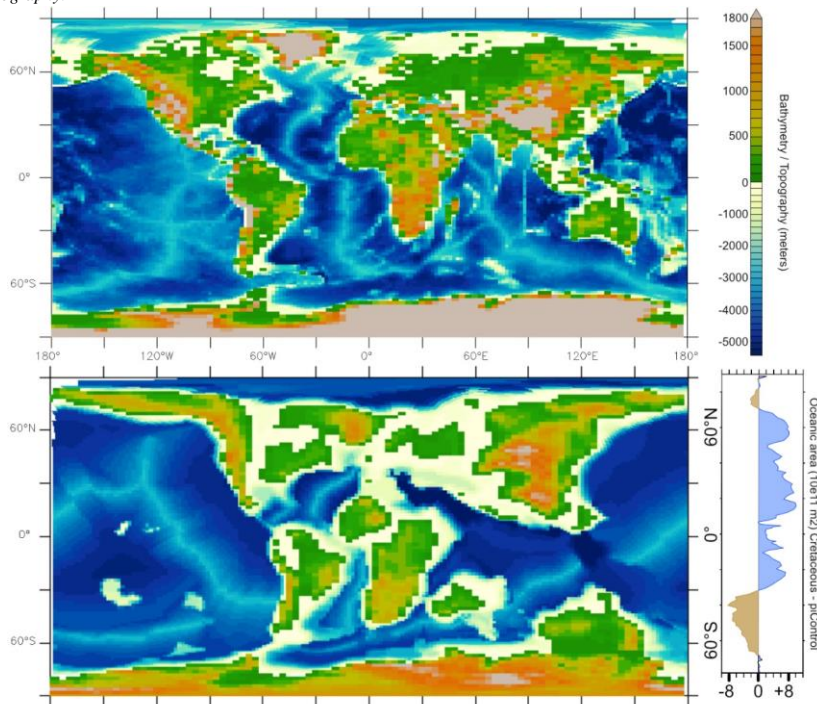


Figure 3: Evolution of Albedo (surface and planetary) and emissivity, in percentages and of T2M (°C) from piControl to 4X-CRETACEOUS simulations. The major change is always recorded with the change of pCO₂ between 1X-NOICE and 4X-NOICE simulations.

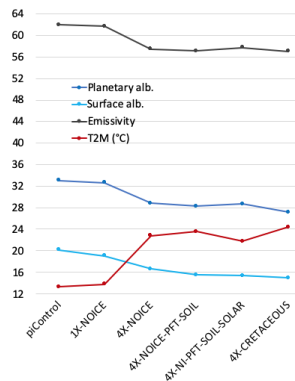
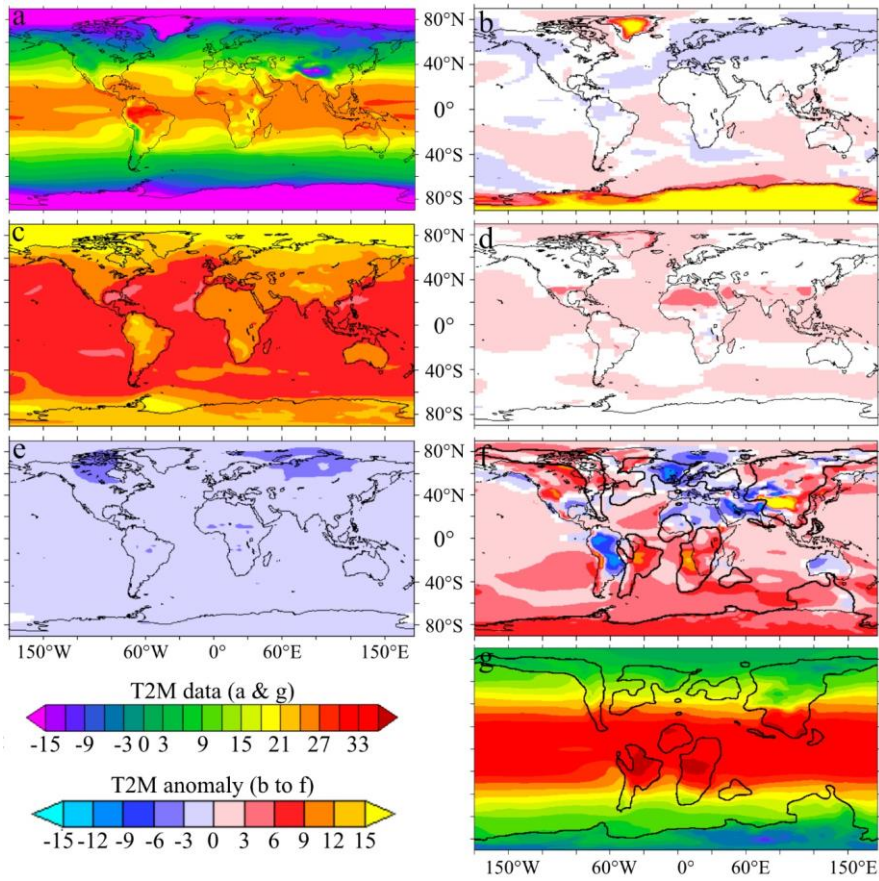


Figure 4: T2M (°C) for (a) piControl initial simulation and (g) Cretaceous final simulation, and anomalies (°C) for intermediate simulations: (b) 1X-NOICE-piControl, (c) 4X-NOICE-1X-NOICE, (d) 4X-NOICE-PFT-SOIL – 4X-NOICE, (e) 4X-NOICE-PFT-SOIL-SOLAR – 4X-NOICE-PFT-SOIL, (f) 4X-CRETACEOUS - 4X-NOICE-PFT-SOIL. White color (not represented in the colourbar) correspond to areas where the anomaly is not statistically significant according to the student test.



590
 591
 592
 593
 594
 595
 596
 597
 598
 599
 600

Figure 5: Mean annual cloudiness for 1X-NOICE and 4X-NOICE simulations. (a) Anomaly of total cloudiness (4X-NOICE – 1X-NOICE). (b) Low-altitude cloudiness (Below 680 hPa of atmospheric pressure - solid curves) and high-altitude cloudiness Above 440 hPa of atmospheric pressure - dashed curves) for 1X-NOICE (black) and 4X-NOICE (red) simulations.

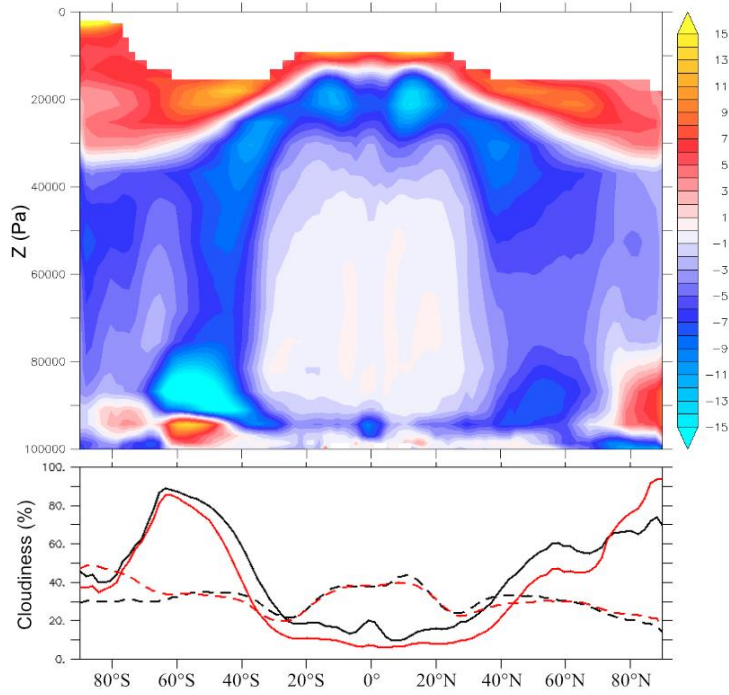


Figure 6: T2M (°C) mean annual meridional gradients for 4X-NI-PFT-SOIL-SOLAR (black) and 4X-CRETACEOUS (red) simulations. Solid curve corresponds to annual average, dashed curves correspond to winter and summer values. The 4X-CRETACEOUS simulation is generally warmer than the 4X-NI-PFT-SOIL-SOLAR-SOLAR simulation, with the exception of the boreal summer.

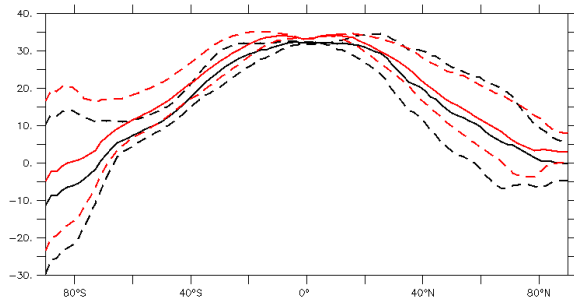
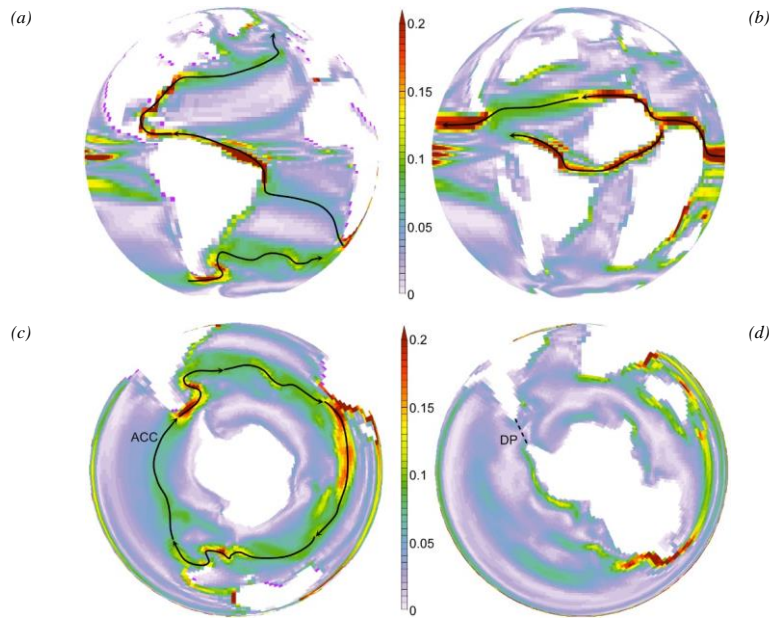


Figure 7: Surface currents for 4X-NOICE-PFT-SOIL-SOLAR (left) and 4X-CRETACEOUS (right) simulations. (a), (b) Intensity of surface circulation (Sv – Annual Mean for 0-80 meters of water depth). Strong equatorial winds lead to the

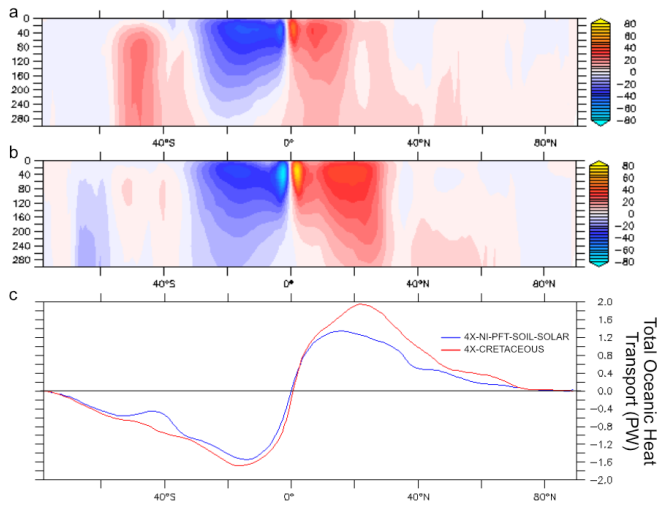
601

formation of an equatorial circumglobal current. (c), (d) Intensity of surface circulation (S_v – Annual Mean for 0-80 meters of water depth). The closure of the Drake passage (DP-300 meters of water depth) leads to the suppression of the ACC.

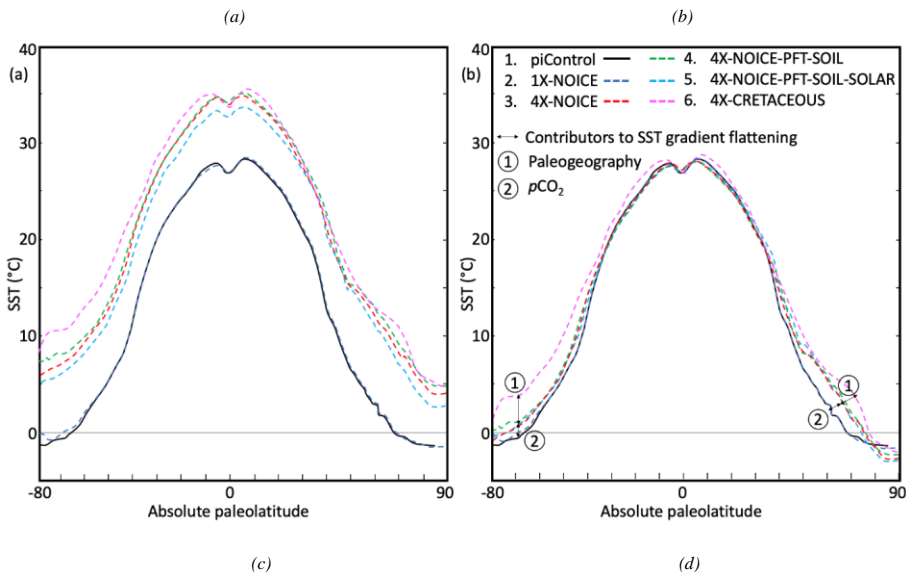


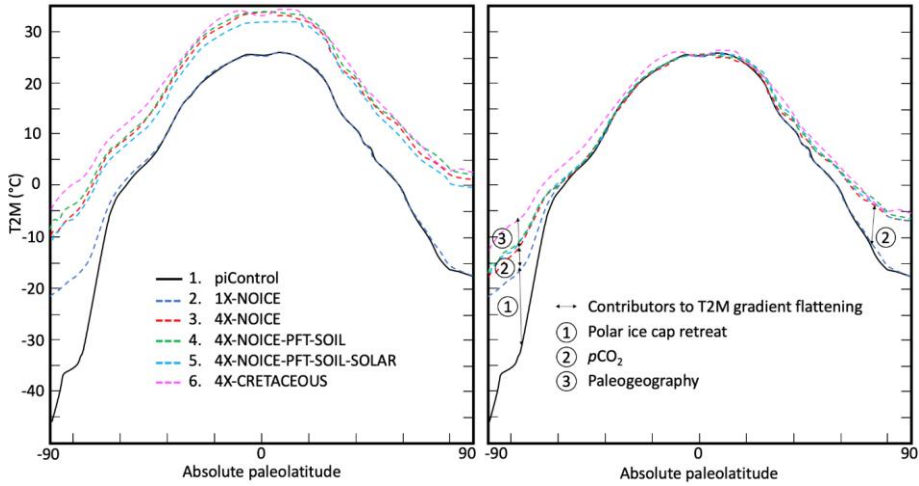
602
603
604
605
606
607
608
609
610
611
612
613
614
615
616
617

Figure 8 - (a), (b) Global mean annual meridional stream-function (S_v) for the first 300 meters of water depth. Red and blue colors indicate clockwise and anti-clockwise circulation respectively. (a): 4X-NI-PFT-SOIL-SOLAR and (b) 4X-CRETACEOUS. (c) Oceanic heat transport for 4X-NI-PFT-SOIL-SOLAR and 4X-CRETACEOUS simulations. Positive and negative values indicate northward and southward transport direction, respectively.



618
 619
 620 *Figure 9: (a) Mean annual meridional Sea-Surface Temperature gradients for all simulations. (b) Same SST curves than (a)*
 621 *but superimposed such as equator temperatures are equal, allowing to compare the steepness of the curves. (c) Meridional*
 622 *atmospheric surface temperature gradients for all simulations. (d) Same curves than (c) but superimposed such as equator*
 623 *temperatures are equal.*





624
625
626
627
628
629
630
631
632
633

634 Figure 10: Meridional surface temperature gradients for the 4X-CRETACEOUS simulation. (a) Oceanic temperatures: the
 635 solid line corresponds to the mean annual temperature obtained from the modeling. Dashed lines correspond to winter and
 636 summer seasonal averages. The grey shaded areas correspond to local monthly temperatures. Data points are obtained with
 637 several proxies for the Cenomano-Turonian period. The green data point is obtained from TEX 86 for the Maastrichtian (70
 638 Ma) and extrapolated for 90 Ma. The Huber et al. (2018) point is obtained from $\delta^{18}O$ on foraminifera and the Vandenmark et
 639 al., 2007 point is interpreted from the presence of crocodylian fossils. MAT=Mean Annual Temperature, CM=Coldest Month.
 640 (b) Atmospheric temperatures: same legend as (a) for modeled temperatures. Data points are obtained from several proxies
 641 including CLAMP analysis on paleofloras, leaf analyses, paleosol-derived climofunction or bioclimatic analysis. Symbols
 642 represent mean annual temperatures and solid lines associated ranges/errors. Dashed lines represent monthly mean
 643 temperatures. Orange data points are for Cenomano-Turonian ages (100-90 Ma), blue data points for Albian and green data
 644 points for Coniacian-Santonian (88-85 Ma).

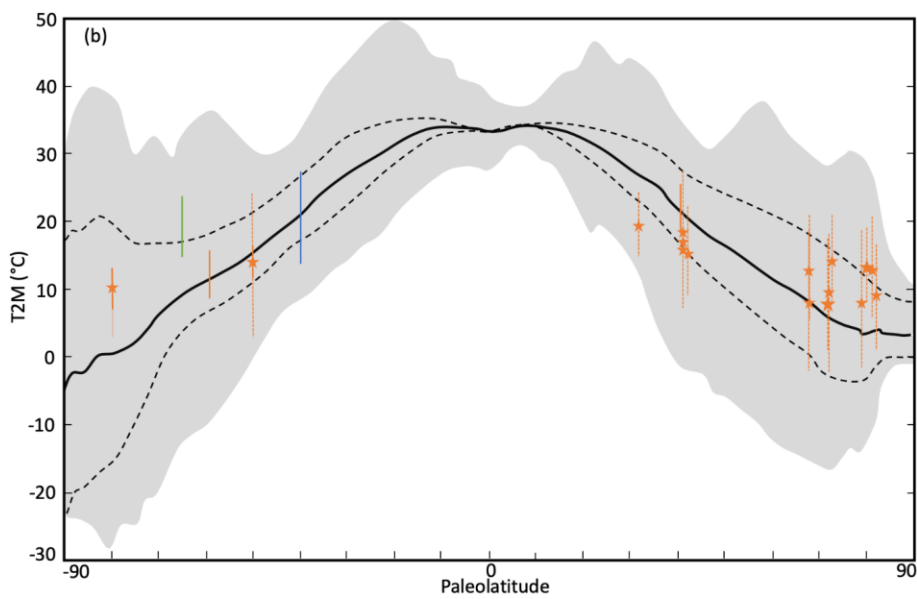
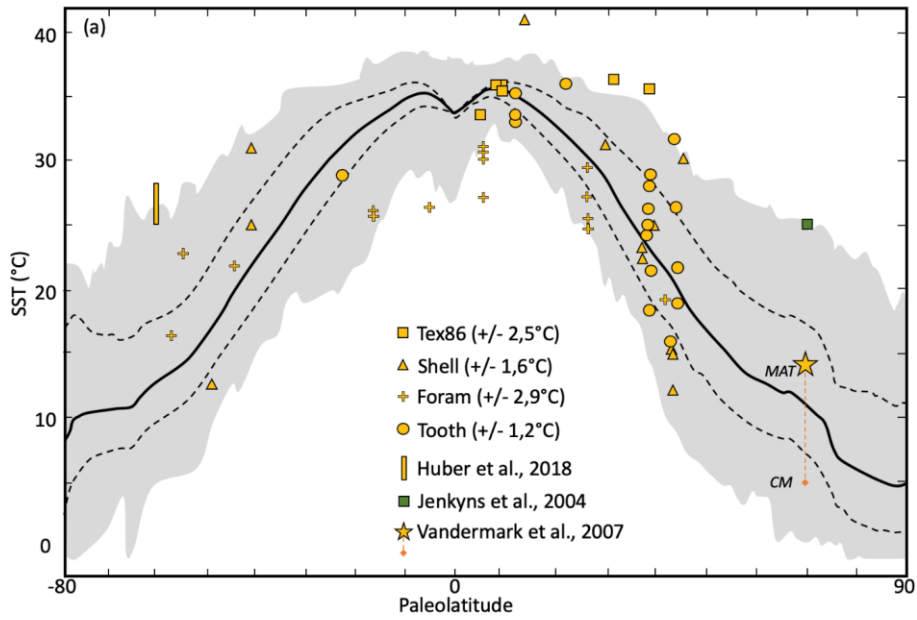
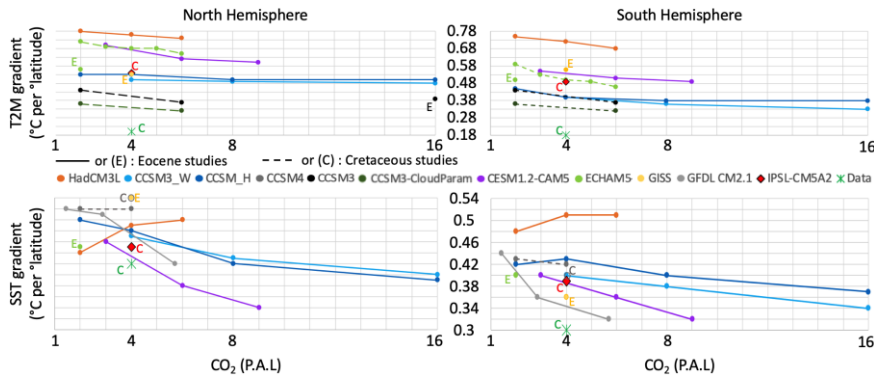


Figure 11: Plot of atmospheric and sea surface mean annual temperature gradients vs pCO₂ for different modelling studies and data compilation. Data gradients are plotted for a default pCO₂ value of 4 P.A.L. Gradients are expressed in °C per °latitude and are calculated from 30 to 80 degrees of latitude. Gradients linked by a line correspond to studies realized with the same model & paleogeography. Solid lines or gradients marked with a (E) correspond to an Eocene paleogeography. Dashed lines or gradients marked with a C correspond to a Cretaceous paleogeography.



645

646

647 REFERENCES

648

649 Aumont, O. and Bopp, L.: Globalizing results from ocean in situ iron fertilization studies,
650 Global Biogeochem. Cycles, 20(2), 1–15, doi:10.1029/2005GB002591, 2006.

651 Aumont, O., Ethé, C., Tagliabue, A., Bopp, L. and Gehlen, M.: PISCES-v2: An ocean
652 biogeochemical model for carbon and ecosystem studies, Geosci. Model Dev., 8(8), 2465–
653 2513, doi:10.5194/gmd-8-2465-2015, 2015.

654 Barclay, R. S., McElwain, J. C. and Sageman, B. B.: Carbon sequestration activated by a
655 volcanic CO₂ pulse during Ocean Anoxic Event 2, Nat. Geosci., 3(3), 205–208,
656 doi:10.1038/ngeo757, 2010.

657 Barron, E. J.: Model simulations of Cretaceous climates : the role of geography and carbon
658 dioxide, , 1(1989), 1993.

659 Barron, E. J., Fawcett, P. J., Peterson, W. H., Pollard, D. and Thompson, S. L.: A " simulation
660 " of mid-Cretaceous climate Abstract . A series of general circulation model experiments W
661 increased from present day). By combining all three major variables levels of CO₂ . Four
662 times present-day • s W provided the best match to the this, , 10(5), 953–962, 1995.

663 Van Bentum, E. C., Reichart, G. J., Forster, A. and Sinninghe Damsté, J. S.: Latitudinal
664 differences in the amplitude of the OAE-2 carbon isotopic excursion: PCO₂and paleo

665 productivity, *Biogeosciences*, 9(2), 717–731, doi:10.5194/bg-9-717-2012, 2012.

666 Berner, R. A.: GEOCARBSULF: A combined model for Phanerozoic atmospheric O₂ and
667 CO₂, *Geochim. Cosmochim. Acta*, 70(23 SPEC. ISS.), 5653–5664,
668 doi:10.1016/j.gca.2005.11.032, 2006.

669 Bice, K. L. and Norris, R. D.: Possible atmospheric CO₂ extremes of the Middle Cretaceous
670 (late Albian-Turonian), *Paleoceanography*, 17(4), 22-1-22–17, doi:10.1029/2002pa000778,
671 2003.

672 Bice, K. L., Birgel, D., Meyers, P. A., Dahl, K. A., Hinrichs, K. U. and Norris, R. D.: A
673 multiple proxy and model study of Cretaceous upper ocean temperatures and atmospheric
674 CO₂ concentrations, *Paleoceanography*, 21(2), 1–17, doi:10.1029/2005PA001203, 2006.

675 Bopp, L., Resplandy, L., Orr, J. C., Doney, S. C., Dunne, J. P., Gehlen, M., Halloran, P.,
676 Heinze, C., Ilyina, T., Séférian, R., Tjiputra, J. and Vichi, M.: Multiple stressors of ocean
677 ecosystems in the 21st century: Projections with CMIP5 models, *Biogeosciences*, 10(10),
678 6225–6245, doi:10.5194/bg-10-6225-2013, 2013.

679 Bopp, L., Resplandy, L., Untersee, A., Le Mezo, P. and Kageyama, M.: Ocean
680 (de)oxygenation from the Last Glacial Maximum to the twenty-first century: Insights from
681 Earth System models, *Philos. Trans. R. Soc. A Math. Phys. Eng. Sci.*, 375(2102),
682 doi:10.1098/rsta.2016.0323, 2017.

683 Brady, E. C., Deconto, R. M. and Thompson, S. L.: Deep Water Formation and Poleward
684 Ocean Heat Transport in the Warm Climate Extreme of the Cretaceous (80 Ma) evidence, ,
685 25(22), 4205–4208, 1998.

686 Broccoli, A. J. and Manabe, S.: The influence of continental ice, atmospheric CO₂, and land
687 albedo on the climate of the last glacial maximum, *Clim. Dyn.*, 1(2), 87–99,
688 doi:10.1007/BF01054478, 1987.

689 Bush, A. B. G., George, S. and Philander, H.: The late Cretaceous ' Simulation with a coupled
690 atmosphere-ocean general circulation model, , 12(3), 495–516, 1997.

691 Charney, J., Arakawa, A., Baker, D. ., Bolin, B., Dickinson, R. E., Goody, R. ., Leith, C. .,
692 Stommel, H. . and Wunsch, C. .: Carbon Dioxide and Climate, National Academies Press,
693 Washington, D.C., 1979.

694 Contoux, C., Jost, A., Ramstein, G., Sepulchre, P., Krinner, G. and Schuster, M.: Megalake
695 chad impact on climate and vegetation during the late Pliocene and the mid-Holocene, *Clim.*
696 *Past*, 9(4), 1417–1430, doi:10.5194/cp-9-1417-2013, 2013.

697 Contoux, C., Dumas, C., Ramstein, G., Jost, A. and Dolan, A. M.: Modelling Greenland ice
698 sheet inception and sustainability during the Late Pliocene, *Earth Planet. Sci. Lett.*, 424, 295–

699 305, doi:10.1016/j.epsl.2015.05.018, 2015.

700 Crowley, T. J. and Berner, R. A.: CO₂ and climate change, *Science* (80-.), 292(5518), 870–
701 872, doi:10.1126/science.1061664, 2001.

702 Crowley, T. J. and Zachos, J. C.: Comparison of zonal temperature profiles for past warm
703 time periods, in *Warm Climates in Earth History*, edited by B. T. Huber, K. G. Macleod, and
704 S. L. Wing, pp. 50–76, Cambridge University Press, Cambridge., 1999.

705 Crowley, T. J., Short, D. A., Mengel, J. G. and North, G. R.: Role of seasonality in the
706 evolution of climate during the last 100 million years, *Science* (80-.), 231(4738), 579–584,
707 doi:10.1126/science.231.4738.579, 1986.

708 Damsté, J. S. S., Kuypers, M. M. M., Pancost, R. D. and Schouten, S.: The carbon isotopic
709 response of algae, (cyano)bacteria, archaea and higher plants to the late Cenomanian
710 perturbation of the global carbon cycle: Insights from biomarkers in black shales from the
711 Cape Verde Basin (DSDP Site 367), *Org. Geochem.*, 39(12), 1703–1718,
712 doi:10.1016/j.orggeochem.2008.01.012, 2008.

713 Deconto, R. M., Brady, E. C., Bergengren, J. and Hay, W. W.: Late Cretaceous climate,
714 vegetation, and ocean interactions, *Warm Clim. Earth Hist.*, 275–296,
715 doi:10.1017/cbo9780511564512.010, 2000.

716 Von Deimling, T. S., Ganopolski, A., Held, H. and Rahmstorf, S.: How cold was the last
717 Glacial maximum?, *Geophys. Res. Lett.*, 33(14), 1–5, doi:10.1029/2006GL026484, 2006.

718 Donnadieu, Y., Pierrehumbert, R., Jacob, R. and Fluteau, F.: Modelling the primary control of
719 paleogeography on Cretaceous climate, *Earth Planet. Sci. Lett.*, 248(1–2), 411–422,
720 doi:10.1016/j.epsl.2006.06.007, 2006.

721 Dufresne, J. L., Foujols, M. A., Denvil, S., Caubel, A., Marti, O., Aumont, O., Balkanski, Y.,
722 Bekki, S., Bellenger, H., Benshila, R., Bony, S., Bopp, L., Braconnot, P., Brockmann, P.,
723 Cadule, P., Cheruy, F., Codron, F., Cozic, A., Cugnet, D., de Noblet, N., Duvel, J. P., Ethé,
724 C., Fairhead, L., Fichefet, T., Flavoni, S., Friedlingstein, P., Grandpeix, J. Y., Guez, L.,
725 Guilyardi, E., Hauglustaine, D., Hourdin, F., Idelkadi, A., Ghattas, J., Joussaume, S.,
726 Kageyama, M., Krinner, G., Labetoulle, S., Lahellec, A., Lefebvre, M. P., Lefevre, F., Levy,
727 C., Li, Z. X., Lloyd, J., Lott, F., Madec, G., Mancip, M., Marchand, M., Masson, S.,
728 Meurdesoif, Y., Mignot, J., Musat, I., Parouty, S., Polcher, J., Rio, C., Schulz, M.,
729 Swingedouw, D., Szopa, S., Talandier, C., Terray, P., Viovy, N. and Vuichard, N.: Climate
730 change projections using the IPSL-CM5 Earth System Model: From CMIP3 to CMIP5., 2013.

731 Egbert, G. D., Ray, R. D. and Bills, B. G.: Numerical modeling of the global semidiurnal tide
732 in the present day and in the last glacial maximum, *J. Geophys. Res. C Ocean.*, 109(3), 1–15,

733 doi:10.1029/2003jc001973, 2004.

734 Enderton, D. and Marshall, J.: Explorations of Atmosphere–Ocean–Ice Climates on an
735 Aquaplanet and Their Meridional Energy Transports, *J. Atmos. Sci.*, 66(6), 1593–1611,
736 doi:10.1175/2008jas2680.1, 2008.

737 Fichefet, T. and Maqueda, M. A. M.: Sensitivity of a global sea ice model to the treatment of
738 ice thermodynamics and dynamics, *J. Geophys. Res. Ocean.*, 102(C6), 12609–12646,
739 doi:10.1029/97JC00480, 1997.

740 Fletcher, B. J., Brentnall, S. J., Quick, W. P. and Beerling, D. J.: BRYOCARB: A process-
741 based model of thallose liverwort carbon isotope fractionation in response to CO₂, O₂, light
742 and temperature, *Geochim. Cosmochim. Acta*, 70(23 SPEC. ISS.), 5676–5691,
743 doi:10.1016/j.gca.2006.01.031, 2006.

744 Fluteau, F., Ramstein, G., Besse, J., Guiraud, R. and Masse, J. P.: Impacts of palaeogeography
745 and sea level changes on Mid-Cretaceous climate, *Palaeogeogr. Palaeoclimatol. Palaeoecol.*,
746 247(3–4), 357–381, doi:10.1016/j.palaeo.2006.11.016, 2007.

747 Foster, G. L., Royer, D. L. and Lunt, D. J.: Future climate forcing potentially without
748 precedent in the last 420 million years, *Nat. Commun.*, 8, 1–8, doi:10.1038/ncomms14845,
749 2017.

750 Friedrich, O., Norris, R. D. and Erbacher, J.: Evolution of middle to late Cretaceous oceans—A
751 55 m.y. Record of Earth’s temperature and carbon cycle, *Geology*, 40(2), 107–110,
752 doi:10.1130/G32701.1, 2012.

753 Gastineau, G., D’Andrea, F. and Frankignoul, C.: Atmospheric response to the North Atlantic
754 Ocean variability on seasonal to decadal time scales, *Clim. Dyn.*, 40(9–10), 2311–2330,
755 doi:10.1007/s00382-012-1333-0, 2013.

756 Gates, W. L., Boyle, J. S., Covey, C., Dease, C. G., Doutriaux, C. M., Drach, R. S., Fiorino,
757 M., Gleckler, P. J., Hnilo, J. J., Marlais, S. M., Phillips, T. J., Potter, G. L., Santer, B. D.,
758 Sperber, K. R., Taylor, K. E. and Williams, D. N.: An Overview of the Results of the
759 Atmospheric Model Intercomparison Project (AMIP I), *Bull. Am. Meteorol. Soc.*, 80(1), 29–
760 55 [online] Available from: <http://www.jstor.org/stable/26214897>, 1999.

761 Godd ris, Y., Donnadi u, Y., Le Hir, G., Lefebvre, V. and Nardin, E.: The role of
762 palaeogeography in the Phanerozoic history of atmospheric CO₂ and climate, *Earth-Science
763 Rev.*, 128, 122–138, doi:10.1016/j.earscirev.2013.11.004, 2014.

764 Golaz, J., Caldwell, P. M., Van Roekel, L. P., Petersen, M. R., Tang, Q., Wolfe, J. D.,
765 Abeshu, G., Anantharaj, V., Asay-Davis, X. S., Bader, D. C., Baldwin, S. A., Bisht, G.,
766 Bogenschutz, P. A., Branstetter, M., Brunke, M. A., Brus, S. R., Burrows, S. M., Cameron-

767 Smith, P. J., Donahue, A. S., Deakin, M., Easter, R. C., Evans, K. J., Feng, Y., Flanner, M.,
768 Foucar, J. G., Fyke, J. G., Griffin, B. M., Hannay, C., Harrop, B. E., Hunke, E. C., Jacob, R.
769 L., Jacobsen, D. W., Jeffery, N., Jones, P. W., Keen, N. D., Klein, S. A., Larson, V. E.,
770 Leung, L. R., Li, H., Lin, W., Lipscomb, W. H., Ma, P., Mahajan, S., Maltrud, M. E.,
771 Mametjanov, A., McClean, J. L., McCoy, R. B., Neale, R. B., Price, S. F., Qian, Y., Rasch, P.
772 J., Reeves Eyre, J. E. J., Riley, W. J., Ringler, T. D., Roberts, A. F., Roesler, E. L., Salinger,
773 A. G., Shaheen, Z., Shi, X., Singh, B., Tang, J., Taylor, M. A., Thornton, P. E., Turner, A. K.,
774 Veneziani, M., Wan, H., Wang, H., Wang, S., Williams, D. N., Wolfram, P. J., Worley, P. H.,
775 Xie, S., Yang, Y., Yoon, J., Zelinka, M. D., Zender, C. S., Zeng, X., Zhang, C., Zhang, K.,
776 Zhang, Y., Zheng, X., Zhou, T. and Zhu, Q.: The DOE E3SM coupled model version 1:
777 Overview and evaluation at standard resolution, *J. Adv. Model. Earth Syst.*, 1–82,
778 doi:10.1029/2018ms001603, 2019.
779 Goldner, A., Herold, N. and Huber, M.: Antarctic glaciation caused ocean circulation changes
780 at the Eocene-Oligocene transition, *Nature*, 511(7511), 574–577, doi:10.1038/nature13597,
781 2014.
782 Gough: Solar interior structure variations*, *Sol. Phys.*, 74(September 1980), 21–34, 1981.
783 Green, J. A. M. and Huber, M.: Tidal dissipation in the early Eocene and implications for
784 ocean mixing, *Geophys. Res. Lett.*, 40(11), 2707–2713, doi:10.1002/grl.50510, 2013.
785 Gyllenhaal, E. D., Engberts, C. J., Markwick, P. J., Smith, L. H. and Patzkowsky, M. E.: The
786 Fujita-Ziegler model: a new semi-quantitative technique for estimating paleoclimate from
787 paleogeographic maps, *Palaeogeogr. Palaeoclimatol. Palaeoecol.*, 86(1–2), 41–66,
788 doi:10.1016/0031-0182(91)90005-C, 1991.
789 Hay, W. W., DeConto, R. M., de Boer, P., Flögel, S., Song, Y. and Stepashko, A.: Possible
790 solutions to several enigmas of Cretaceous climate, Springer Berlin Heidelberg., 2019.
791 Heinemann, M., Jungclauss, J. H. and Marotzke, J.: Warm Paleocene/Eocene climate as
792 simulated in ECHAM5/MPI-OM, *Clim. Past*, 5(4), 785–802, doi:10.5194/cp-5-785-2009,
793 2009.
794 Herman, A. B. and Spicer, R. A.: Palaeobotanical evidence for a warm Cretaceous Arctic
795 Ocean, *Nature*, 380(6572), 330–333, doi:10.1038/380330a0, 1996.
796 Herman, A. B. and Spicer, R. A.: Mid-Cretaceous floras and climate of the Russian high
797 Arctic (Novosibirsk Islands, Northern Yakutiya), *Palaeogeogr. Palaeoclimatol. Palaeoecol.*,
798 295(3–4), 409–422, doi:10.1016/j.palaeo.2010.02.034, 2010.
799 Herweijer, C., Seager, R., Winton, M. and Clement, A.: Why ocean heat transport warms the
800 global mean climate, *Tellus, Ser. A Dyn. Meteorol. Oceanogr.*, 57(4), 662–675,

801 doi:10.1111/j.1600-0870.2005.00121.x, 2005.

802 Hollis, C. J., Taylor, K. W. R., Handley, L., Pancost, R. D., Huber, M., Creech, J. B., Hines,
803 B. R., Crouch, E. M., Morgans, H. E. G., Crampton, J. S., Gibbs, S., Pearson, P. N. and
804 Zachos, J. C.: Early Paleogene temperature history of the Southwest Pacific Ocean :
805 Reconciling proxies and models, *Earth Planet. Sci. Lett.*, 349–350, 53–66,
806 doi:10.1016/j.epsl.2012.06.024, 2012.

807 Hong, S. K. and Lee, Y. Il: Evaluation of atmospheric carbon dioxide concentrations during
808 the Cretaceous, *Earth Planet. Sci. Lett.*, 327–328, 23–28, doi:10.1016/j.epsl.2012.01.014,
809 2012.

810 Hotinski, R. M. and Toggweiler, J. R.: Impact of a Tethyan circumglobal passage on ocean
811 heat transport and “equable” climates, *Paleoceanography*, 18(1), n/a-n/a,
812 doi:10.1029/2001PA000730, 2003.

813 Hourdin, F., Foujols, M. A., Codron, F., Guemas, V., Dufresne, J. L., Bony, S., Denvil, S.,
814 Guez, L., Lott, F., Ghattas, J., Braconnot, P., Marti, O., Meurdesoif, Y. and Bopp, L.: Impact
815 of the LMDZ atmospheric grid configuration on the climate and sensitivity of the IPSL-
816 CM5A coupled model, *Clim. Dyn.*, 40(9–10), 2167–2192, doi:10.1007/s00382-012-1411-3,
817 2013.

818 Huber, B. T., Hodell, D. A. and Hamilton, C. P.: ... Late Cretaceous climate of the southern
819 high latitudes: Stable isotopic evidence for minimal ..., *Geol. Soc. Am. Bull.*, (10), 1164–
820 1191, doi:10.1130/0016-7606(1995)107<1164, 1995.

821 Huber, B. T., Leckie, R. M., Norris, R. D., Bralower, T. J. and CoBabe, E.: Foraminiferal
822 assemblage and stable isotopic change across the Cenomanian-Turonian boundary in the
823 Subtropical North Atlantic, *J. Foraminifer. Res.*, 29(4), 392–417, 1999.

824 Huber, B. T., Norris, R. D. and MacLeod, K. G.: Deep-sea paleotemperature record of
825 extreme warmth during the Cretaceous, *Geology*, 30(2), 123–126, doi:10.1130/0091-
826 7613(2002)030<0123:DSPROE>2.0.CO;2, 2002.

827 Huber, B. T., MacLeod, K. G., Watkins, D. K. and Coffin, M. F.: The rise and fall of the
828 Cretaceous Hot Greenhouse climate, *Glob. Planet. Change*, 167(April), 1–23,
829 doi:10.1016/j.gloplacha.2018.04.004, 2018.

830 Huber, M.: Progress in Greenhouse Climate Modeling, *Paleontol. Soc. Pap.*, 18, 213–262,
831 doi:10.1017/s108933260000262x, 2012.

832 Huber, M. and Caballero, R.: The early Eocene equable climate problem revisited, *Clim. Past*,
833 7(2), 603–633, doi:10.5194/cp-7-603-2011, 2011.

834 Hunter, S. J., Haywood, A. M., Valdes, P. J., Francis, J. E. and Pound, M. J.: Modelling

835 equable climates of the Late Cretaceous: Can new boundary conditions resolve data-model
836 discrepancies?, *Palaeogeogr. Palaeoclimatol. Palaeoecol.*, 392, 41–51,
837 doi:10.1016/j.palaeo.2013.08.009, 2013.

838 Hutchinson, D. K., De Boer, A. M., Coxall, H. K., Caballero, R., Nilsson, J. and Baatsen, M.:
839 Climate sensitivity and meridional overturning circulation in the late Eocene using GFDL
840 CM2.1, *Clim. Past*, 14(6), 789–810, doi:10.5194/cp-14-789-2018, 2018.

841 IPCC: Climate Change 2014: Synthesis Report. Contribution of Working Groups I, II and III
842 to the Fifth Assessment Report of the Intergovernmental Panel on Climate Change., 2014.

843 Jenkyns, H. C.: Geochemistry of oceanic anoxic events, *Geochemistry, Geophys.*
844 *Geosystems*, 11(3), 1–30, doi:10.1029/2009GC002788, 2010.

845 Jenkyns, H. C., Forster, A., Schouten, S. and Sinninghe Damsté, J. S.: High temperatures in
846 the Late Cretaceous Arctic Ocean, *Nature*, 432(7019), 888–892, doi:10.1038/nature03143,
847 2004.

848 Kageyama, M., Braconnot, P., Bopp, L., Caubel, A., Foujols, M. A., Guilyardi, E., Khodri,
849 M., Lloyd, J., Lombard, F., Mariotti, V., Marti, O., Roy, T. and Woillez, M. N.: Mid-
850 Holocene and Last Glacial Maximum climate simulations with the IPSL model-part I:
851 Comparing IPSL_CM5A to IPSL_CM4, *Clim. Dyn.*, 40(9–10), 2447–2468,
852 doi:10.1007/s00382-012-1488-8, 2013.

853 Kennedy, A. T., Farnsworth, A., Lunt, D. J., Lear, C. H. and Markwick, P. J.: Atmospheric
854 and oceanic impacts of Antarctic glaciation across the Eocene-Oligocene transition, *Philos.*
855 *Trans. R. Soc. A Math. Phys. Eng. Sci.*, 373(2054), doi:10.1098/rsta.2014.0419, 2015.

856 Kerr, A. C. and Kerr, A. C.: Oceanic plateau formation : A cause of mass extinction and black
857 shale deposition around the Cenomanian-Turonian boundary ? Oceanic plateau formation : a
858 cause of mass extinction and black shale deposition around the Cenomanian – Turonian
859 boundary ?, , (May), doi:10.1144/gsjgs.155.4.0619, 1998.

860 Knorr, G. and Lohmann, G.: Climate warming during antarctic ice sheet expansion at the
861 middle miocene transition, *Nat. Geosci.*, 7(5), 376–381, doi:10.1038/ngeo2119, 2014.

862 Koch-Larrouy, A., Madec, G., Bouruet-Aubertot, P., Gerkema, T., Bessières, L. and Molcard,
863 R.: On the transformation of Pacific Water into Indonesian Throughflow Water by internal
864 tidal mixing, *Geophys. Res. Lett.*, 34(4), 1–6, doi:10.1029/2006GL028405, 2007.

865 Krinner, G., Viovy, N., de Noblet-Ducoudré, N., Ogée, J., Polcher, J., Friedlingstein, P.,
866 Ciais, P., Sitch, S. and Prentice, I. C.: A dynamic global vegetation model for studies of the
867 coupled atmosphere-biosphere system, *Global Biogeochem. Cycles*, 19(1), 1–33,
868 doi:10.1029/2003GB002199, 2005.

869 Ladant, J. B. and Donnadieu, Y.: Palaeogeographic regulation of glacial events during the
870 Cretaceous supergreenhouse, *Nat. Commun.*, 7(April 2017), 1–9, doi:10.1038/ncomms12771,
871 2016.

872 Ladant, J. B., Donnadieu, Y., Bopp, L., Lear, C. H. and Wilson, P. A.: Meridional Contrasts
873 in Productivity Changes Driven by the Opening of Drake Passage, *Paleoceanogr.*
874 *Paleoclimatology*, 302–317, doi:10.1002/2017PA003211, 2018.

875 de Lavergne, C., Falahat, S., Madec, G., Roquet, F., Nycander, J. and Vic, C.: Toward global
876 maps of internal tide energy sinks, *Ocean Model.*, 137(April), 52–75,
877 doi:10.1016/j.ocemod.2019.03.010, 2019.

878 Leier, A., Quade, J., DeCelles, P. and Kapp, P.: Stable isotopic results from paleosol
879 carbonate in South Asia: Paleoenvironmental reconstructions and selective alteration, *Earth*
880 *Planet. Sci. Lett.*, 279(3–4), 242–254, doi:10.1016/j.epsl.2008.12.044, 2009.

881 Levine, X. J. and Schneider, T.: Response of the Hadley Circulation to Climate Change in an
882 Aquaplanet GCM Coupled to a Simple Representation of Ocean Heat Transport, *J. Atmos.*
883 *Sci.*, 68(4), 769–783, doi:10.1175/2010jas3553.1, 2010.

884 Littler, K., Robinson, S. A., Bown, P. R., Nederbragt, A. J. and Pancost, R. D.: High sea-
885 surface temperatures during the Early Cretaceous Epoch, *Nat. Geosci.*, 4(3), 169–172,
886 doi:10.1038/ngeo1081, 2011.

887 Lunt, D. J., Jones, T. D., Heinemann, M., Huber, M., LeGrande, A., Winguth, A., Loptson,
888 C., Marotzke, J., Roberts, C. D., Tindall, J., Valdes, P. and Winguth, C.: A model-data
889 comparison for a multi-model ensemble of early Eocene atmosphere-ocean simulations:
890 EoMIP, *Clim. Past*, 8(5), 1717–1736, doi:10.5194/cp-8-1717-2012, 2012a.

891 Lunt, D. J., Haywood, A. M., Schmidt, G. A., Salzmann, U., Valdes, P. J., Dowsett, H. J. and
892 Loptson, C. A.: On the causes of mid-Pliocene warmth and polar amplification, *Earth Planet.*
893 *Sci. Lett.*, 321–322, 128–138, doi:10.1016/j.epsl.2011.12.042, 2012b.

894 Lunt, D. J., Farnsworth, A., Loptson, C., L Foster, G., Markwick, P., O’Brien, C. L., Pancost,
895 R. D., Robinson, S. A. and Wrobel, N.: Palaeogeographic controls on climate and proxy
896 interpretation, *Clim. Past*, 12(5), 1181–1198, doi:10.5194/cp-12-1181-2016, 2016.

897 Lunt, D. J., Huber, M., Anagnostou, E., Baatsen, M. L. J., Caballero, R., DeConto, R.,
898 Dijkstra, H. A., Donnadieu, Y., Evans, D., Feng, R., Foster, G. L., Gasson, E., Von Der
899 Heydt, A. S., Hollis, C. J., Inglis, G. N., Jones, S. M., Kiehl, J., Turner, S. K., Korty, R. L.,
900 Kozdon, R., Krishnan, S., Ladant, J. B., Langebroek, P., Lear, C. H., LeGrande, A. N., Littler,
901 K., Markwick, P., Otto-Bliesner, B., Pearson, P., Poulsen, C. J., Salzmann, U., Shields, C.,
902 Snell, K., Stärz, M., Super, J., Tabor, C., Tierney, J. E., Tourte, G. J. L., Tripathi, A.,

903 Upchurch, G. R., Wade, B. S., Wing, S. L., Winguth, A. M. E., Wright, N. M., Zachos, J. C.
904 and Zeebe, R. E.: The DeepMIP contribution to PMIP4: Experimental design for model
905 simulations of the EECO, PETM, and pre-PETM (version 1.0), *Geosci. Model Dev.*, 10(2),
906 889–901, doi:10.5194/gmd-10-889-2017, 2017.

907 MacLeod, K. G., Huber, B. T., Berrocoso, Á. J. and Wendler, I.: A stable and hot Turonian
908 without glacial $\delta^{18}\text{O}$ excursions is indicated by exquisitely preserved Tanzanian foraminifera,
909 *Geology*, 41(10), 1083–1086, doi:10.1130/G34510.1, 2013.

910 Madec, G.: NEMO ocean engine (2012), , (27), 2012.

911 Madec, G. and Imbard, M.: A global ocean mesh to overcome the North Pole singularity,
912 *Clim. Dyn.*, 12(6), 381–388, doi:10.1007/BF00211684, 1996.

913 Maffre, P., Ladant, J. B., Donnadieu, Y., Sepulchre, P. and Godd ris, Y.: The influence of
914 orography on modern ocean circulation, *Clim. Dyn.*, 50(3–4), 1277–1289,
915 doi:10.1007/s00382-017-3683-0, 2018.

916 Mays, C., Steinhorsdottir, M. and Stilwell, J. D.: Climatic implications of Ginkgoites
917 *waarrensis* Douglas emend. from the south polar Tupuangi flora, Late Cretaceous
918 (Cenomanian), Chatham Islands, *Palaeogeogr. Palaeoclimatol. Palaeoecol.*, 438, 308–326,
919 doi:10.1016/j.palaeo.2015.08.011, 2015.

920 Le M zo, P., Beaufort, L., Bopp, L., Braconnot, P. and Kageyama, M.: From monsoon to
921 marine productivity in the Arabian Sea: Insights from glacial and interglacial climates, *Clim.*
922 *Past*, 13(7), 759–778, doi:10.5194/cp-13-759-2017, 2017.

923 Monteiro, F. M., Pancost, R. D., Ridgwell, A. and Donnadieu, Y.: Nutrients as the dominant
924 control on the spread of anoxia and euxinia across the Cenomanian-Turonian oceanic anoxic
925 event (OAE2): Model-data comparison, *Paleoceanography*, 27(4), 1–17,
926 doi:10.1029/2012PA002351, 2012.

927 M ller, R. D., Sdrolias, M., Gaina, C. and Roest, W. R.: Age, spreading rates, and spreading
928 asymmetry of the world’s ocean crust, *Geochemistry, Geophys. Geosystems*, 9(4), 1–19,
929 doi:10.1029/2007GC001743, 2008.

930 Niezgodzki, I., Knorr, G., Lohmann, G., Tyszka, J. and Markwick, P. J.: Late Cretaceous
931 climate simulations with different CO₂ levels and subarctic gateway configurations: A model-
932 data comparison, *Paleoceanography*, 32(9), 980–998, doi:10.1002/2016PA003055, 2017.

933 Norris, R. D., Bice, K. L., Magno, E. A. and Wilson, P. A.: Jiggling the tropical thermostat in
934 the Cretaceous hothouse, *Geology*, 30(4), 299–302, doi:10.1130/0091-
935 7613(2002)030<0299:JTTTTIT>2.0.CO;2, 2002.

936 O’Brien, C. L., Robinson, S. A., Pancost, R. D., Sinninghe Damst , J. S., Schouten, S., Lunt,

937 D. J., Alsenz, H., Bornemann, A., Bottini, C., Brassell, S. C., Farnsworth, A., Forster, A.,
938 Huber, B. T., Inglis, G. N., Jenkyns, H. C., Linnert, C., Littler, K., Markwick, P., McAnena,
939 A., Mutterlose, J., Naafs, B. D. A., Püttmann, W., Sluijs, A., van Helmond, N. A. G. M.,
940 Vellekoop, J., Wagner, T. and Wrobel, N. E.: Cretaceous sea-surface temperature evolution:
941 Constraints from TEX 86 and planktonic foraminiferal oxygen isotopes, *Earth-Science Rev.*,
942 172(March 2016), 224–247, doi:10.1016/j.earscirev.2017.07.012, 2017.

943 Ohba, M. and Ueda, H.: A GCM Study on Effects of Continental Drift on Tropical Climate at
944 the Early and Late Cretaceous, *J. Meteorol. Soc. Japan*, 88(6), 869–881,
945 doi:10.2151/jmsj.2010-601, 2011.

946 Ortega, P., Mignot, J., Swingedouw, D., Sévellec, F. and Guilyardi, E.: Reconciling two
947 alternative mechanisms behind bi-decadal variability in the North Atlantic, *Prog. Oceanogr.*,
948 137, 237–249, doi:10.1016/j.pocean.2015.06.009, 2015.

949 Otto-bliesner, B. L. and Upchurch, G. R.: the Late Cretaceous period, , 385127(February),
950 18–21, 1997.

951 Pearson, P. N., Ditchfield Peter, W., Singano Joyce, Harcourt-Brown Katherine, G.,
952 Nicholas Christopher, J., Olsson Richard, K., Shackleton Nicholas, J. and Hall Mike, A.:
953 erratum: Warm tropical sea surface temperatures in the Late Cretaceous and Eocene epochs,
954 *Nature*, 414(6862), 470 [online] Available from: <http://dx.doi.org/10.1038/35106617>, 2001.

955 Poulsen, C. J., Seidov, D., Barron, E. J. and Peterson, W. H.: The impact of paleogeographic
956 evolution on the surface oceanic circulation and the marine environment within the Mid-
957 Cretaceous tethys, , 13(5), 546–559, 1998.

958 Poulsen, C. J., Barron, E. J., Arthur, M. A. and Peterson, W. H.: Response of the mid-
959 Cretaceous global oceanic circulation to tectonic and CO₂ forcings,
960 *Paleoceanography*, 16(6), 576–592, doi:10.1029/2000PA000579, 2001.

961 Poulsen, C. J., Gendaszek, A. S. and Jacob, R. L.: Did the rifting of the Atlantic Ocean cause
962 the Cretaceous thermal maximum?, *Geology*, 31(2), 115–118, doi:10.1130/0091-
963 7613(2003)031<0115:DTROTA>2.0.CO;2, 2003.

964 Poulsen, C. J., Pollard, D. and White, T. S.: General circulation model simulation of the δ18O
965 content of continental precipitation in the middle Cretaceous: A model-proxy comparison,
966 *Geology*, 35(3), 199–202, doi:10.1130/G23343A.1, 2007.

967 Pucéat, E., Lécuyer, C., Donnadieu, Y., Naveau, P., Cappetta, H., Ramstein, G., Huber, B. T.
968 and Kriwet, J.: Fish tooth δ18O revising Late Cretaceous meridional upper ocean water
969 temperature gradients, *Geology*, 35(2), 107–110, doi:10.1130/G23103A.1, 2007.

970 Retallack, G. J. and Conde, G. D.: Deep time perspective on rising atmospheric CO₂, *Glob.*

971 Planet. Change, 189(March), 103177, doi:10.1016/j.gloplacha.2020.103177, 2020.

972 Robinson, S. A., Dickson, A. J., Pain, A., Jenkyns, H. C., O'Brien, C. L., Farnsworth, A. and
 973 Lunt, D. J.: Southern Hemisphere sea-surface temperatures during the Cenomanian-Turonian:
 974 Implications for the termination of Oceanic Anoxic Event 2, *Geology*, 47(2), 131–134,
 975 doi:10.1130/G45842.1, 2019.

976 Rose, B. E. J. and Ferreira, D.: Ocean heat transport and water vapor greenhouse in a warm
 977 equable climate: A new look at the low gradient paradox, *J. Clim.*, 26(6), 2117–2136,
 978 doi:10.1175/JCLI-D-11-00547.1, 2013.

979 Royer, D. L.: *Atmospheric CO₂ and O₂ During the Phanerozoic: Tools, Patterns, and*
 980 *Impacts*, 2nd ed., Elsevier Ltd., 2013.

981 Royer, D. L., Berner, R. A. and Park, J.: Climate sensitivity constrained by CO₂
 982 concentrations over the past 420 million years, *Nature*, 446(7135), 530–532,
 983 doi:10.1038/nature05699, 2007.

984 Sandler, A. and Harlavan, Y.: Early diagenetic illitization of illite-smectite in Cretaceous
 985 sediments (Israel): evidence from K-Ar dating, *Clay Miner.*, 41(2), 637–658,
 986 doi:10.1180/0009855064120210, 2006.

987 Sarr, A. C., Sepulchre, P. and Husson, L.: Impact of the Sunda Shelf on the Climate of the
 988 Maritime Continent, *J. Geophys. Res. Atmos.*, doi:10.1029/2018JD029971, 2019.

989 Schmidt, G. A. and Mysak, L. A.: Can increased poleward oceanic heat flux explain the warm
 990 Cretaceous climate?, *Paleoceanography*, 11(5), 579–593, doi:10.1029/96PA01851, 1996.

991 Sellers, P. ., Bounoua, L., Collatz, G. J., Randall, D. A., Dazlich, D. A., Los, S. O., Berry, J.
 992 A., Fung, I., Tucker, C. J., Field, C. B. and Jensen, T. G.: Comparison of Radiative and
 993 Physiological Effects of Doubled Atmospheric CO₂ on Climate, , 1402–1406, 1996.

994 Sellwood, B. W., Price, G. D. and Valdest, P. J.: Cretaceous temperatures, , 370(August),
 995 453–455, 1994.

996 Sepulchre, P., Caubel, A., Ladant, J., Bopp, L., Boucher, O., Braconnot, P., Brockmann, P.,
 997 Cozic, A., Donnadieu, Y., Estella-perez, V., Ethé, C., Fluteau, F., Foujols, M., Gastineau, G.,
 998 Ghattas, J., Hauglustaine, D., Hourdin, F., Kageyama, M., Khodri, M., Marti, O., Meurdesoif,
 999 Y., Mignot, J., Sarr, A., Servonnat, J., Swingedouw, D., Szopa, S. and Tardif, D.: IPSL-
 1000 CM5A2 . An Earth System Model designed for multi-millennial climate simulations, ,
 1001 (December), 2019.

1002 Sewall, J. O., Van De Wal, R. S. W., Van Der Zwan, K., Van Oosterhout, C., Dijkstra, H. A.
 1003 and Scotese, C. R.: Climate model boundary conditions for four Cretaceous time slices, *Clim.*
 1004 *Past*, 3(4), 647–657, doi:10.5194/cp-3-647-2007, 2007.

1005 Simmons, H. L., Jayne, S. R., St. Laurent, L. C. and Weaver, A. J.: Tidally driven mixing in a
1006 numerical model of the ocean general circulation, *Ocean Model.*, 6(3–4), 245–263,
1007 doi:10.1016/S1463-5003(03)00011-8, 2004.

1008 Sluijs, A., Schouten, S., Pagani, M., Woltering, M. and Brinkhuis, H.: Subtropical Arctic
1009 Ocean temperatures during the Palaeocene / Eocene thermal maximum, , (May 2014),
1010 doi:10.1038/nature04668, 2006.

1011 Spicer, R. A. and Herman, A. B.: The Late Cretaceous environment of the Arctic: A
1012 quantitative reassessment based on plant fossils, *Palaeogeogr. Palaeoclimatol. Palaeoecol.*,
1013 295(3–4), 423–442, doi:10.1016/j.palaeo.2010.02.025, 2010.

1014 Steinig, S., Dumann, W., Park, W., Latif, M., Kusch, S., Hofmann, P. and Flögel, S.:
1015 Evidence for a regional warm bias in the Early Cretaceous TEX86 record, *Earth Planet. Sci.*
1016 *Lett.*, 539, 116184, doi:10.1016/j.epsl.2020.116184, 2020.

1017 Swingedouw, D., Rodehacke, C. B., Olsen, S. M., Menary, M., Gao, Y., Mikolajewicz, U.
1018 and Mignot, J.: On the reduced sensitivity of the Atlantic overturning to Greenland ice sheet
1019 melting in projections: a multi-model assessment, *Clim. Dyn.*, 44(11–12), 3261–3279,
1020 doi:10.1007/s00382-014-2270-x, 2015.

1021 Swingedouw, D., Mignot, J., Guilyardi, E., Nguyen, S. and Ormières, L.: Tentative
1022 reconstruction of the 1998–2012 hiatus in global temperature warming using the IPSL–
1023 CM5A–LR climate model, *Comptes Rendus - Geosci.*, 349(8), 369–379,
1024 doi:10.1016/j.crte.2017.09.014, 2017.

1025 Tabor, C. R., Poulsen, C. J., Lunt, D. J., Rosenbloom, N. A., Otto-Bliesner, B. L., Markwick,
1026 P. J., Brady, E. C., Farnsworth, A. and Feng, R.: The cause of Late Cretaceous cooling: A
1027 multimodel-proxy comparison, *Geology*, 44(11), 963–966, doi:10.1130/G38363.1, 2016.

1028 Tagliabue, A., Bopp, L., Dutay, J. C., Bowie, A. R., Chever, F., Jean-Baptiste, P., Bucciarelli,
1029 E., Lannuzel, D., Remenyi, T., Sarthou, G., Aumont, O., Gehlen, M. and Jeandel, C.:
1030 Hydrothermal contribution to the oceanic dissolved iron inventory, *Nat. Geosci.*, 3(4), 252–
1031 256, doi:10.1038/ngeo818, 2010.

1032 Tan, N., Ramstein, G., Dumas, C., Contoux, C., Ladant, J. B., Sepulchre, P., Zhang, Z. and
1033 De Schepper, S.: Exploring the MIS M2 glaciation occurring during a warm and high
1034 atmospheric CO₂ Pliocene background climate, *Earth Planet. Sci. Lett.*, 472, 266–276,
1035 doi:10.1016/j.epsl.2017.04.050, 2017.

1036 Tierney, J. E.: GDGT Thermometry: Lipid Tools for Reconstructing Paleotemperatures,
1037 *Paleontol. Soc. Pap.*, 18, 115–132, doi:10.1017/s1089332600002588, 2012.

1038 Turgeon, S. C. and Creaser, R. A.: Cretaceous oceanic anoxic event 2 triggered by a massive

1039 magmatic episode, , 454(July), doi:10.1038/nature07076, 2008.

1040 Upchurch, G. R.: Vegetation-atmosphere interactions and their role in global warming during
1041 the latest Cretaceous, *Philos. Trans. R. Soc. B Biol. Sci.*, 353(1365), 97–112,
1042 doi:10.1098/rstb.1998.0194, 1998.

1043 Upchurch, G. R., Kiehl, J., Shields, C., Scherer, J. and Scotese, C.: Latitudinal temperature
1044 gradients and high-latitude temperatures during the latest Cretaceous: Congruence of geologic
1045 data and climate models, *Geology*, 43(8), 683–686, doi:10.1130/G36802.1, 2015.

1046 Valcke, S., Budich, R., Carter, M., Guilyardi, E., Lautenschlager, M., Redler, R. and
1047 Steenman-clark, L.: The PRISM software framework and the OASIS coupler, , 5(September
1048 2014), 2001–2004, 2006.

1049 Vandermark, D., Tarduno, J. A. and Brinkman, D. B.: A fossil champsosaur population from
1050 the high Arctic: Implications for Late Cretaceous paleotemperatures, *Palaeogeogr.*
1051 *Palaeoclimatol. Palaeoecol.*, 248(1–2), 49–59, doi:10.1016/j.palaeo.2006.11.008, 2007.

1052 Veizer, J., Godderis, Y. and François, L. M.: Evidence for decoupling of atmospheric CO₂
1053 and global climate during the Phanerozoic eon, *Nature*, 408(6813), 698–701,
1054 doi:10.1038/35047044, 2000.

1055 Wang, Y., Huang, C., Sun, B., Quan, C., Wu, J. and Lin, Z.: Paleo-CO₂ variation trends and
1056 the Cretaceous greenhouse climate, *Earth-Science Rev.*, 129, 136–147,
1057 doi:10.1016/j.earscirev.2013.11.001, 2014.

1058 Wilson, M. F. and Henderson-sellers, A.: LBA Regional Vegetation and Soils, 1-Degree
1059 (Wilson and Henderson-Sellers), , doi:10.3334/ORNLDAAC/687, 2003.

1060 Woillez, M. N., Levvasseur, G., Daniau, A. L., Kageyama, M., Urrego, D. H., Sánchez-
1061 Goñi, M. F. and Hanquiez, V.: Impact of precession on the climate, vegetation and fire
1062 activity in southern Africa during MIS4, *Clim. Past*, 10(3), 1165–1182, doi:10.5194/cp-10-
1063 1165-2014, 2014.

1064 Zhou, J., Poulsen, C. J., Pollard, D. and White, T. S.: Simulation of modern and middle
1065 Cretaceous marine $\delta^{18}O$ with an ocean-atmosphere general circulation model,
1066 *Paleoceanography*, 23(3), 1–11, doi:10.1029/2008PA001596, 2008.

1067 Zhou, J., Poulsen, C. J., Rosenbloom, N., Shields, C. and Briegleb, B.: Vegetation-climate
1068 interactions in the warm mid-Cretaceous, *Clim. Past*, 8(2), 565–576, doi:10.5194/cp-8-565-
1069 2012, 2012.

1070 Zhu, J., Poulsen, C. J. and Tierney, J. E.: Simulation of Eocene extreme warmth and high
1071 climate sensitivity through cloud feedbacks, *Sci. Adv.*, 5(9), eaax1874,
1072 doi:10.1126/sciadv.aax1874, 2019.

1073 Zhu, J., Poulsen, C. J., Otto-Bliesner, B. L., Liu, Z., Brady, E. C. and Noone, D. C.:
1074 Simulation of early Eocene water isotopes using an Earth system model and its implication
1075 for past climate reconstruction, *Earth Planet. Sci. Lett.*, 537, 116164,
1076 doi:10.1016/j.epsl.2020.116164, 2020.
1077 Zobler, L.: Global Soil Types, 1-Degree Grid (Zobler), , doi:10.3334/ORNLDAAAC/418,
1078 1999.
1079
1080
1081